Influence of geometrical configuration on low angular momentum relativistic accretion around rotating black holes

Pratik Tarafdar[*]
S. N. Bose National Centre For Basic Sciences, Block-JD, Sector-III, Salt Lake, Kolkata 700106, India

Deepika A. Bollimpalli[†]
Harish-Chandra Research Institute, HBNI, Chhatnag Road, Jhunsi, Allahabad 211109, India

Sankhasubhra Nag[‡]
Sarojini Naidu College for Women, 30, Jessore Road, Kolkata 700028, India

Tapas K. Das[§]
Harish-Chandra Research Institute, HBNI, Chhatnag Road, Jhunsi, Allahabad 211109, India

(Received 4 September 2018; published 23 August 2019)

We illustrate how the formation of energy-preserving shocks for polytropic accretion and temperature-preserving shocks for isothermal accretion are influenced by various geometrical configurations of general relativistic, axisymmetric, low angular momentum flow in the Kerr metric. Relevant pre- and postshock states of the accreting fluid, both dynamical and thermodynamic, are studied comprehensively. Self-gravitational backreaction on the metric is not considered in the present context. An elegant eigenvalue-based analytical method is introduced to provide qualitative descriptions of the phase orbits corresponding to stationary transonic accretion solutions without resorting to involved numerical schemes. Effort is made to understand how the weakly rotating flow behaves in close proximity to the event horizon and how such "quasiterminal" quantities are influenced by the black hole spin for different matter geometries. Our main purpose is thus to mathematically demonstrate that, for non-self-gravitating accretion, separate matter geometries, in addition to the corresponding space-time geometry, control various shock-induced phenomena observed within black hole accretion disks. We expect to reveal how such phenomena observed near the horizon depend on the physical environment of the source harboring a supermassive black hole at its center. We also expect to unfold correspondences between the dependence of accretion-related parameters on flow geometries and on black hole spin. Temperature-preserving shocks in isothermal accretion may appear bright, as a substantial amount of rest-mass energy of the infalling matter gets dissipated at the shock surface, and the prompt removal of such energy to maintain isothermality may power the x-ray/IR flares emitted from our Galactic Center.

DOI: 10.1103/PhysRevD.100.043024

I. INTRODUCTION

Study of the accretion process helps in observational identification of black hole candidates. The dynamical and thermodynamic properties of such an accretion flow reveal the extreme nature of space-time surrounding black holes. The emergent spectra from the accretion process is used to probe the characteristic features of the black hole metric [1]. It is thus imperative to understand the dynamics of the relativistic black hole accretion phenomenon.

In order to satisfy the inner boundary condition imposed by the black hole event horizon, black hole accretion usually manifests transonic properties, until the source of accreting matter is perceived to be supersonic stellar wind. The transonic mechanism is simple—accreting matter starts subsonically from a large distance and becomes supersonic in the course of its motion since it has to cross the event horizon supersonically. The maximum relativistic sound speed allowed for the steepest possible equation of state is $c/\sqrt{3}$, whereas the bulk velocity of the infalling matter

[*]pratikta16@gmail.com
[†]deepika@camk.edu.pl
Present address: Nicolaus Copernicus Astronomical Centre, Polish Academy of Sciences, ul. Bartycka, 00-716, Warsaw, Poland.
[‡]sankha@sncwgs.ac.in
[§]Corresponding author.
tapas@hri.res.in
Also at Physics and Applied Mathematics Unit, Indian Statistical Institute, Kolkata 700108, India.

while crossing the horizon should reach the velocity of light [2]. Hence, black hole accretion of initially subsonic matter is necessarily transonic [3]. The location at which such change of state of "sonicity" takes place is called the *sonic point*.

Whether the steady state accretion flow may encounter more than one sonic point depends on the angular momentum content of the flow. For reasonably low angular momentum sub-Keplerian flow (the value of the specific angular momentum is not sufficient for the flow to form a closed stable circular orbit at a large distance from the black hole) with *advective velocity* (almost radial velocity owing to sub-Keplerian flow initialized with some nonzero value at a large distance from the black hole leading to advection towards the event horizon), usually more than one sonic transition is possible, and the flow may become multitransonic provided that a stationary shock may develop to join the stationary integral flow solutions passing through the aforementioned sonic points. Such low angular momentum flow is common in nature (for instance, accretion onto the supermassive black hole situated at the center of our Galaxy), and a host of literature is available where such shocked multitransonic accretion has been studied in detail (see Refs. [4–39] and the references therein).

The epoch making recent discovery regarding the observational evidence of black holes through shadow imaging [40–45] clearly indicates that it is imperative to study the dynamical and thermodynamic states of matter very close to the black hole event horizon. In this connection, it is important to understand the dynamical behavior of low angular momentum shocked multitransonic flow at the extremely close vicinity of the event horizon in order to demonstrate the shadow image for flow onto Sgr A$*$, since accretion onto our Galactic Center black hole is supposed to be weakly rotating low angular momentum flow [34,46–55]. Apart from the astrophysical aspects, study of the physics of transonic black hole accretion has recently found importance in dynamical systems theory as well. Attempts have been made to understand the astrophysical black hole system as an example of relativistic fluid flow under the strong gravitational field where the critical point analysis of dynamical systems theory can find its application. Analytical methods from the theory of dynamical systems have been borrowed in the context of investigating general accretion problems [56–59]. A few earlier works have even explored this approach while studying the problem of astrophysical accretion [9,13,60].

It is thus tempting to observe whether one can provide a combined treatment of relativistic black hole accretion where both the astrophysical context and the dynamical systems features of the flow can be investigated *simultaneously.* In this interdisciplinary work, we make such an attempt to illustrate the properties of accreting black hole systems from a broader perspective. We study steady state accretion disk models with various geometrical configurations of accreting material. For stationary integral solutions of such low angular momentum accretion, we show that the space derivatives of the dynamical flow velocities and that of the sound speed may be expressed by a set of coupled first order ordinary differential equations which can be readily mapped onto the equations governing an autonomous dynamical system, and we borrow the techniques of critical point analysis from dynamical systems theory to identify the transonic point(s) of the flow. Various related concepts of dynamical systems theory which are applied in this article will be clarified in subsequent sections. Once the sonic points have been identified, we analyze the dependence of the flow profile on the geometric configuration of the accretion disk. A more detailed description of what we plan to do in this work is provided in Sec. III.

II. CONNECTION TO DYNAMICAL SYSTEMS

The number of dynamical physical systems and their respective phase-space plots are innumerably large. There exist such points on phase-space diagrams which might attract or repel the *phase trajectories* of a system; i.e., all possible trajectories on the respective phase space either converge onto these points or diverge from them. A system resting on such a point, upon being subjected to small local perturbations, would either restabilize to its unperturbed state or destabilize away from it. Such points are called *critical points* or *fixed points* or *stable points* or *equilibrium points* or *stationary points* of the system. In order to avoid any confusion, we would like to inform the reader that these terms, wherever used in this article, should be considered synonymous. Depending on dimensions of the system, the natures of the critical points in its phase space are equally diverse. In our work, we encounter the emergence of *center-type* and *saddle-type* critical points only. Had it been a case of viscous flows, we would have to deal with *spiral-type* critical points as well. Center-type points are forbidden from phase-space trajectories, and the system keeps oscillating around them. The equilibrium points of conservative simple harmonic oscillators are typical examples of center-type critical points. For saddle-type critical points, a system rests upon a very delicate equilibrium. Depending on the direction of perturbation, the system might either return to the stable point or fly away from it. The phase portraits pertaining to the physical systems of interest display combinations of center- and saddle-type critical points, as will be shown in the subsequent sections.

The reason behind devoting a whole section to critical points is that the fundamental idea of our work is to analyze black hole accretion from the perspective of the theory of dynamical systems, and the concept of critical points is central to it. Since this work is primarily concerned with stationary flows, it might naturally seem surprising to try and draw any connection with the theory of *dynamical systems*. However, dynamical systems theory endows us with a rich plethora of elegant analytical methods to study the behavior of critical points of a system, and critical points are particular features of stationary states. Our work is about transonic astrophysical flows, and hence a major portion of it deals with the derivation of results related to *sonic points* of the system, as defined in the previous section, and derivation of the related critical point conditions almost always reveal direct correlations between the critical points and sonic points of the accreting fluid. This connection immediately hints at the applicability of mathematical tools related to stability analysis in the theory of dynamical systems to the seemingly unrelated theory of transonic astrophysical accretion. As a matter of fact, the approach of linear stability analysis of fixed points in problems of general fluid dynamics has been in practice for quite some time [61].

III. PLAN OF WORK

We consider general relativistic axially symmetric stationary integral flow solutions in the Kerr metric. In general, astrophysical black holes are believed to possess nonzero spin angular momentum [62–81], and such spin angular momentum (the Kerr parameter a) assumes a vital role in influencing the various characteristic features of accretion-induced astrophysical phenomena [39]. Attempts to study relativistic low angular momentum accretion of inviscid perfect fluids using hydrodynamical codes [82] bridging analytics and numerical relativity are significant in this context. There have also been recent numerical works regarding accretion onto spinning black holes investigating parameters that might influence the stability, stationarity, and other longtime behaviors of the flow [83–85]. The geometrical configurations of low angular momentum accreting matter may be roughly classified into three different categories. When the thickness of the flow is assumed to be constant with respect to the radial distance, the flow is dubbed "constant height accretion flow." If the flow thickness is not constant at all radial distances but the ratio of the local flow thickness and the radial distance is constant, it is called conical flow, which actually may be considered a quasispherical slowly rotating flow, and such a geometrical configuration is a ideal setup for studying inviscid accretion. For the third category of flow, neither the flow thickness nor the ratio of the local flow thickness to the radial distance remains constant, and the flow assumes a wedgelike structure. Such a geometric configuration remains in hydrostatic equilibrium along the vertical direction, and it will thus be referred to in this work as "flow in vertical equilibrium" for short. Further details about such flows are available in Refs. [2,86–88]. The geometric configurations of flow directly influence the flow properties at close proximity of the event horizon. It is thus imperative to learn how the black hole spin dependence of accretion is influenced by the matter geometry. This is precisely what we would like to explore in this work.

We formulate and solve the general relativistic Euler equation and the continuity equation in the Kerr metric to obtain the stationary integral accretion solutions for the three different geometric configurations (see, e.g., Sec. 4.1 of Ref. [89], and the references therein, for a detailed classification of three such geometries) of low angular momentum axially symmetric advective flow onto spinning black holes. We then study the stationary phase portrait of multitransonic accretion and demonstrate how stationary shocks may form for such flow topologies. Then, we study the astrophysics of shock formation and demonstrate how the Kerr parameter influences the location of the shock formed and other shock-related quantities. We also report on how such spin dependence varies from one type of flow geometry to the other. The overall process to accomplish such a task has been performed in the following way.

We first try to address the issue, to a certain extent, completely analytically. It can be shown that the stationary transonic solutions for inviscid accretion can be mapped as critical solutions onto the phase portrait spanned by radial Mach number, and the corresponding radial distance measured on the equatorial plane [90]. For all three geometries, the Euler and continuity equations are formulated in the Kerr metric. Borrowing relevant methodologies from the theory of dynamical systems, the time-independent parts of these equations are considered in order to locate the corresponding critical/sonic points. One can obtain more than one critical point as well. In such cases, one needs to classify which kinds of critical points they are. We provide an eigenvalue-based analytical method to find out the nature of the critical points and demonstrate that they are either center type or saddle type. What can be done analytically is that once the nature of the critical points is determined following the aforementioned procedures, the tentative nature of corresponding orbits on the phase portrait can be roughly anticipated, and the overall multitransonic phase portraits can be understood. The purview of the analytical regime is limited at this point. The advantage of introducing the eigenvalue-based analytical method is to qualitatively understand how the phase orbits corresponding to the stationary transonic solutions would look, without incorporating any complicated numerical techniques.

The exact shape of the phase orbits, however, can never be obtained analytically. One needs to numerically integrate the Euler and continuity equations to obtain the stationary integral mono-multitransonic solutions. In Sec. VIII, we provide the methodology for integrating the fluid equations to obtain the transonic solutions.

Multitransonic solutions require the presence of a stationary shock to join the integral solutions passing through the outer and inner sonic points, respectively. In Sec. IX, we discuss shock formation phenomena in detail and demonstrate how the Kerr parameter influences the shock-related quantities for three different matter geometries. In Sec. X, the concept of quasiterminal values is introduced to understand how the weakly rotating accretion flow behaves at the extremely close proximity of the event horizon and how such behaviors, for three different matter geometries, are influenced by black hole spin. The subsequent sections deal with a similar line treatment for isothermal flows.

The entire study presented in our work has been divided into six subcategories. We study three different geometrical models of polytropic accretion, then study the same models for isothermal accretion—and for each flow model, we analyze the black hole spin dependence of various flow properties.

Such a comprehensive treatment, although apparently too technical at first sight, is actually useful to the astrophysics community, we believe. Our low angular momentum flow model resembles accretion onto Sgr A∗. Thus, it would not be unreasonable to believe that the theoretical study of shocked multitransonic accretion might be helpful for understanding the black hole spectra of Sgr A∗, as well as for realizing the nature of the shadow image of the corresponding black hole. As of now, no study has been performed on how accretion-induced shock may influence the image of the shadow of the event horizon. Only continuous flows have been studied thus far from the imaging point of view, whereas flows with large scale discontinuities have not yet been investigated. Such an investigation with hot and dense postshock flow may reveal various important features of the shadow image. We will discuss this issue in more detail in the last section in our concluding remarks.

In the context of a very detailed study of the flow for various disk geometries, it is important to note that such flow geometries have been previously considered as theoretical constructs. Since we did not have an observational tool with the necessary high resolving power, there was no option for direct verification of the actual geometric configuration of the flow. However, the recent observation of an actual black hole shadow image has opened up new horizons in this area and may shed some light on this issue. If one studies the dynamical/thermodynamic properties of accretion for all possible geometric configurations, constructs spectra out of it, creates images of the corresponding shadow, and finally compares the details of the theoretical construction with the observed image, it might be possible to answer the following long-standing questions:

(1) What should be the actual geometric shape of the accretion disk?
(2) Of the different proposed theoretical expressions for disk geometry, which one should have the closest resemblance to a realistic flow structure?

We believe that, in this area, our comprehensive work regarding the dependence of flow properties on flow geometries will be beneficial.

IV. POLYTROPIC FLOW STRUCTURES FOR VARIOUS MATTER GEOMETRIES

Before delving into detailed and involved calculations, we shall break down and summarize the whole formalism that has been used for deriving the conditions satisfied at the critical points of polytropic flows with constant height disks (hereafter, CH), quasispherical or conical disks (hereafter, CF), and disks in vertical hydrostatic equilibrium (hereafter, VE) into the following basic steps. The corresponding critical point conditions for isothermal flows shall be derived in relevant sections following a similar method.

(1) We write down the equations for the conserved *specific energy* ($\mathcal{E}$) and the conserved *mass accretion rate* ($\dot{M}$) pertaining to the specific flow. It may be noted that $\mathcal{E}$ remains the same for the CH, CF, and VE disks. Disk geometry influences $\dot{M}$ due only to its dependence on the area of cross section through which influx of matter occurs.
(2) We differentiate the equations for $\mathcal{E}$ and $\dot{M}$ with respect to radial distance r, and we solve simultaneously to obtain expressions for the spatial gradients of the advective velocity u and sound speed c_s.
(3) Expression for spatial gradient of the advective velocity is of the form $du/dr = \mathcal{N}(r, u, c_s)/\mathcal{D}(r, u, c_s)$. Integrating du/dr with proper initial conditions generates the corresponding phase-space plots. Since velocity and their gradients at specific radial distances cannot be readily known without actual numerical integration; hence, the initial conditions required for carrying out the integration are fixed using the values of u, c_s, and du/dr at the critical points r_c given by the critical point conditions. These conditions are obtained by equating $\mathcal{N}$ and $\mathcal{D}$ simultaneously to zero. It is a standard method that has been borrowed from the theory of dynamical systems and their stability [91]. Setting the numerator and denominator to zero simultaneously ensures a smooth and continuous physical transonic flow. For multitransonic flows, the continuity is broken at locations of shock. This issue will be dealt with separately in later sections.

As shown in [92], one needs to obtain the expressions for two first integrals of motion—the conserved specific energy $\mathcal{E}$, which is obtained from integral solutions of the time-independent part of the Euler equation and remains invariant for all three matter geometries, and the mass accretion rate $\dot{M}$, which is obtained from the integral solutions of the time-independent part of the continuity equation and varies with the geometric configuration of matter. We start with the constant height flow and then continue the same for two other flow geometries, i.e., wedge-shaped quasispherical or conical flow, and flow in hydrostatic equilibrium along the vertical direction.

For an ideal fluid, the general relativistic Euler and the continuity equations are obtained through the covariant differentiation of the corresponding energy-momentum tensor,

$$T^{\mu\nu} = (\epsilon + p)v^\mu v^\nu + p g^{\mu\nu}, \quad (1)$$

where

$$\epsilon = \rho + \frac{p}{\gamma - 1} \quad (2)$$

is the energy density (which includes the rest mass energy density and the internal energy density), p is the fluid pressure, and v^μ is the velocity field. Using the Boyer-Lindquist coordinate, one can show [39] that the conserved specific energy defined on the equatorial plane is expressed as

$$\mathcal{E} = \frac{\gamma - 1}{\gamma - (1 + c_s^2)}\sqrt{\frac{1}{1-u^2}\left[\frac{Ar^2\Delta}{A^2 - 4\lambda arA + \lambda^2 r^2(4a^2 - r^2\Delta)}\right]}. \quad (3)$$

In the above expression, γ is the ratio of the two specific heat capacities, C_p and C_v, where an adiabatic equation of state of the form $p = K\rho^\gamma$ has been used ρ being the matter density. c_s denotes the position-dependent adiabatic sound speed, defined as

$$c_s^2 = \left(\frac{\partial p}{\partial \epsilon}\right)_{\text{constant entropy}}. \quad (4)$$

The advective velocity u measured along the equatorial plane can be obtained by solving the following equation:

$$v_t = \sqrt{\frac{g_{t\phi}^2 - g_{tt}g_{\phi\phi}}{(1-\lambda\Omega)(1-u^2)(g_{\phi\phi} + \lambda g_{t\phi})}}, \quad (5)$$

where $(g_{t\phi}, g_{tt}, g_{\phi\phi})$ are the corresponding elements of the metric

$$\begin{aligned} ds^2 &= g_{\mu\nu}dx^\mu dx^\nu \\ &= -\frac{r^2\Delta}{A}dt^2 + \frac{r^2}{\Delta}dr^2 + \frac{A}{r^2}(d\phi - \omega dt) + dz^2, \end{aligned} \quad (6)$$

where the line element has been expressed on the equatorial plane, using the Boyer-Lindquist coordinate, and $\omega = \frac{2ar}{A}$, $\Delta = r^2 - 2r + a^2$, $A = r^4 + r^2a^2 + 2ra^2$. λ and Ω are the specific angular momentum and the angular velocity, respectively, as defined by $\lambda = -\frac{v_\phi}{v_t}$, $\Omega = \frac{v^\phi}{v^t} = -\frac{g_{t\phi}+\lambda g_{tt}}{g_{\phi\phi}+\lambda g_{t\phi}}$. It is to be noted that the expression for $\mathcal{E}$ has been obtained using the natural unit where the radial distance (measured along the equatorial plane) has been scaled by GM_{BH}/c^2, and the dynamical as well as the sound velocity have been scaled by the velocity of light in vacuum c, with M_{BH} being the mass of the black hole considered. We also normalize $G = c = M_{\mathrm{BH}} = 1$.

A. Constant height flow

The mass accretion rate may be obtained as

$$\dot{M}_{CH} = 4\pi\sqrt{\Delta}H\rho\sqrt{\frac{u^2}{1-u^2}}, \quad (7)$$

where H is the radius-independent constant thickness of the accretion disk and $\rho = [\frac{c_s^2(\gamma-1)}{\gamma K(\gamma-1-c_s^2)}]^{\frac{1}{\gamma-1}}$. The corresponding entropy accretion rate may be obtained through the transformation $\dot{\Xi} = \dot{M}(K\gamma)^{\frac{1}{\gamma-1}}$ as

$$\dot{\Xi}_{CH} = 4\pi\sqrt{\Delta}H\left[\frac{c_s^2(\gamma-1)}{\gamma-1-c_s^2}\right]^{\frac{1}{\gamma-1}}\sqrt{\frac{u^2}{1-u^2}}. \quad (8)$$

The idea of an entropy accretion rate was initially proposed in Refs. [4,10] in order to calculate the stationary solutions for low angular momentum nonrelativistic transonic accretion under the influence of [93] pseudo-Newtonian potential onto a nonrotating black hole.

The space gradient of the acoustic velocity as well as the dynamical velocity can be computed as

$$\frac{dc_s}{dr} = \frac{\mathcal{N}_1^{CH}}{\mathcal{D}_1^{CH}}, \quad (9)$$

$$\frac{du}{dr} = \frac{\mathcal{N}_2^{CH}}{\mathcal{D}_2^{CH}}, \quad (10)$$

where $\mathcal{N}_1^{CH} = \frac{-2u}{2(1-u^2)}\frac{du}{dr} - \frac{f'}{2f}$, $\mathcal{D}_1^{CH} = \frac{2c_s}{\gamma-1-c_s^2}$, $\mathcal{N}_2^{CH} = u(1-u^2)[\frac{r-1}{\Delta}c_s^2 - \frac{f'}{2f}]$, $\mathcal{D}_2^{CH} = u^2 - c_s^2$, and $f = \frac{\Delta}{B}$, $B = g_{\phi\phi} + 2\lambda g_{t\phi} + \lambda^2 g_{tt}$, and where f' denotes the space derivative of f, i.e., $\frac{df}{dr}$. Hereafter, the sub-superscripts CH will stand for "constant height."

The critical point conditions may be obtained as

$$u^2|_{r_c} = c_s^2|_{r_c} = \left.\frac{f'}{2f}\right|_{r_c}\frac{\Delta_c}{r_c - 1}. \quad (11)$$

Inserting the critical point conditions into the expression of the conserved specific energy, one can solve the corresponding algebraic equation for a specific set of values of $[\mathcal{E}, \lambda, \gamma, a]$ to obtain the value of the critical point r_c.

The gradient of the sound speed and that of the dynamical velocity can also be evaluated at the critical points as

$$\left.\frac{du}{dr}\right|_{r_c} = -\frac{\beta_{CH}}{2\alpha_{CH}} \pm \frac{1}{2\alpha_{CH}}\sqrt{\beta_{CH}^2 - 4\alpha_{CH}\Gamma_{CH}}, \quad (12)$$

$$\left.\frac{dc_s}{dr}\right|_{r_c} = \left.\frac{\mathcal{N}_1}{\mathcal{D}_1}\right|_{r_c}, \quad (13)$$

where the coefficients α_{CH}, β_{CH}, and Γ_{CH} are given by

$$
\begin{aligned}
\alpha_{CH} &= \left.\frac{\gamma-3c_s^2+1}{(c_s^2-1)^2}\right|_{r_c},\\
\beta_{CH} &= \left.\frac{2c_s(r-1)(c_s^2-\gamma+1)}{(c_s^2-1)(a^2+(r-2)r)}\right|_{r_c},\\
\Gamma_{CH} &= \left.\frac{2(c_s^2-1)(r-1)^2}{(a^2+(r-2)r)^2}\right|_{r_c} - \left.\frac{c_s^2-1}{a^2+(r-2)r}\right|_{r_c} + \left.\frac{c_s^2(r-1)^2(-c_s^2+\gamma-1)}{(a^2+(r-2)r)^2}\right|_{r_c}\\
&\quad - \left[\frac{-\frac{a^2\lambda^4(a^2(r+2)+r^3)}{(a^2(r+2)+\lambda^2 r)^2}+\frac{2a^2\lambda^4(r-2)(a^2+\lambda^2)(a^2(r+2)+r^3)}{(a^2(r+2)+\lambda^2 r)^3}-\frac{a^2\lambda^4(r-2)(a^2+3r^2)}{(a^2(r+2)+\lambda^2 r)^2}+\frac{\lambda^4(a^2+\lambda^2)(r^3-a^2(r^2-8))}{(a^2(r+2)+\lambda^2 r)^2}+\frac{\lambda^4 r(2a^2-3r)}{a^2(r+2)+\lambda^2 r}-2a^2r+4a\lambda r+5r^4}{r^4\left(-\frac{\lambda^4(r-2)(a^2(r+2)+r^3)}{r^3(a^2(r+2)+\lambda^2 r)}+\frac{2a^2}{r}+a^2-\frac{4a\lambda}{r}+r^2\right)}\right]_{r_c}\\
&\quad + \left.\frac{4\left(-\frac{a^2\lambda^4(r-2)(a^2(r+2)+r^3)}{(a^2(r+2)+\lambda^2 r)^2}-a^2r^2+\frac{\lambda^4(a^2(r^2-8)-r^3)}{a^2(r+2)+\lambda^2 r}+2a\lambda r^2+r^5\right)}{r^5\left(-\frac{\lambda^4(r-2)(a^2(r+2)+r^3)}{r^3(a^2(r+2)+\lambda^2 r)}+\frac{2a^2}{r}+a^2-\frac{4a\lambda}{r}+r^2\right)}\right|_{r_c}\\
&\quad + \left[\frac{\begin{array}{c}2(2a^5\lambda r^2(r+2)^2+4a^3\lambda^3 r^3(r+2)+2a^2\lambda^2 r^3(r+2)(r^3-a^2)+\lambda^6(-r)(r^3-a^2(r^2-8))\\ +\lambda^4(a^4(r-3)(r+2)^2-3a^2r^4+r^7)+a^4r^2(r+2)^2(r^3-a^2)+2a\lambda^5 r^4)^2\end{array}}{\begin{array}{c}r^2(a^2(r+2)+\lambda^2 r)^2(a^4(r+2)^2r^2-4a^3\lambda(r+2)r^2\\ +a^2(r+2)(r^5+\lambda^2r^3-\lambda^4(r-2))-4a\lambda^3r^3+\lambda^2r^6-\lambda^4(r-2)r^3)^2\end{array}}\right]_{r_c}.
\end{aligned}
$$

Using numerical techniques, Eqs. (9)–(13) can simultaneously be solved to obtain the phase portrait corresponding to the transonic flow.

B. Conical flow

The corresponding expression for the mass and entropy accretion rates for the conical flow come out to be

$$\dot{M}_{CF} = 4\pi\sqrt{\Delta}\Theta r\rho\sqrt{\frac{u^2}{1-u^2}}, \tag{14}$$

$$\dot{\Xi}_{CF} = 4\pi\sqrt{\Delta}\Theta r\left[\frac{c_s^2(\gamma-1)}{\gamma-1-c_s^2}\right]^{\frac{1}{\gamma-1}}\sqrt{\frac{u^2}{1-u^2}}, \tag{15}$$

where Θ is the solid angle subtended by the accretion disk at the horizon. The space gradient of the sound speed and the flow velocity may be obtained as

$$\frac{dc_s}{dr} = \frac{\mathcal{N}_1^{CF}}{\mathcal{D}_1^{CF}}, \tag{16}$$

$$\frac{du}{dr} = \frac{\mathcal{N}_2^{CF}}{\mathcal{D}_2^{CF}}, \tag{17}$$

where $\mathcal{N}_1^{CF}=\mathcal{N}_1^{CH}$, $\mathcal{D}_1^{CF}=\mathcal{D}_1^{CH}$, $\mathcal{N}_2^{CF} = u(1-u^2)\times[\frac{2r^2-3r+a^2}{\Delta r}c_s^2 - \frac{f'}{2f}]$, $\mathcal{D}_2^{CF} = u^2 - c_s^2$, $f = \frac{\Delta}{B}$, $B = g_{\phi\phi} + 2\lambda g_{t\phi} + \lambda^2 g_{tt}$, where the sub-superscripts CF stand for "conical flow."

Hence, the corresponding critical point condition comes out to be

$$u^2|_{r_c} = c_s^2|_{r_c} = \left.\frac{f'}{2f}\right|_{r_c}\frac{\Delta_c r_c}{2r_c^2 - 3r_c + a^2}. \tag{18}$$

Substituting the critical point conditions into the expression of the conserved specific energy, one can solve the corresponding algebraic equation for a specific set of values of $[\mathcal{E},\lambda,\gamma,a]$ to obtain the value of the critical point r_c. The space gradient of c_s and u at the critical points may be obtained as

$$\left.\frac{du}{dr}\right|_{r_c} = -\frac{\beta_{CF}}{2\alpha_{CF}} \pm \frac{1}{2\alpha_{CF}}\sqrt{\beta_{CF}^2 - 4\alpha_{CF}\Gamma_{CF}}, \tag{19}$$

$$\left.\frac{dc_s}{dr}\right|_{r_c} = \left.\frac{\mathcal{N}_1^{CF}}{\mathcal{D}_1^{CF}}\right|_{r_c}, \tag{20}$$

where the coefficients α_{CF}, β_{CF}, and Γ_{CF} are given by

$$\alpha_{CF} = \alpha_{CH},$$

$$\beta_{CF} = \left.\frac{2c_s(a^2+r(2r-3))(c_s^2-\gamma+1)}{(c_s^2-1)r(a^2+(r-2)r)}\right|_{r_c},$$

$$\begin{aligned}\Gamma_{CF} = &-\left.\frac{c_s^2-1}{a^2+(r-2)r}\right|_{r_c} + \left.\frac{2(c_s^2-1)(r-1)^2}{(a^2+(r-2)r)^2}\right|_{r_c} + \left.\frac{c_s^2}{r^2}\right|_{r_c} + \left.\frac{c_s^2(r-1)(a^2+r(2r-3))(c_s^2-\gamma+1)}{(c_s^2-1)r(a^2+(r-2)r)^2}\right|_{r_c} + \left.\frac{c_s^2(-c_s^2+\gamma-1)}{r^2}\right|_{r_c} \\ &+ \left.\frac{c_s^2(r-1)(-c_s^2+\gamma-1)}{r(a^2+(r-2)r)}\right|_{r_c} + \left.\frac{c_s^4(r-1)(a^2+r(2r-3))(-c_s^2+\gamma-1)}{(c_s^2-1)r(a^2+(r-2)r)^2}\right|_{r_c} \\ &- \left[\frac{\begin{matrix}-\frac{a^2\lambda^4(a^2(r+2)+r^3)}{(a^2(r+2)+\lambda^2 r)^2} + \frac{2a^2\lambda^4(r-2)(a^2+\lambda^2)(a^2(r+2)+r^3)}{(a^2(r+2)+\lambda^2 r)^3} - \frac{a^2\lambda^4(r-2)(a^2+3r^2)}{(a^2(r+2)+\lambda^2 r)^2} \\ + \frac{\lambda^4(a^2+\lambda^2)(r^3-a^2(r^2-8))}{(a^2(r+2)+\lambda^2 r)^2} + \frac{\lambda^4 r(2a^2-3r)}{a^2(r+2)+\lambda^2 r} - 2a^2 r + 4a\lambda r + 5r^4\end{matrix}}{r^4(-\frac{\lambda^4(r-2)(a^2(r+2)+r^3)}{r^3(a^2(r+2)+\lambda^2 r)} + \frac{2a^2}{r} + a^2 - \frac{4a\lambda}{r} + r^2)}\right]_{r_c} \\ &+ \left.\frac{4\left(-\frac{a^2\lambda^4(r-2)(a^2(r+2)+r^3)}{(a^2(r+2)+\lambda^2 r)^2} - a^2r^2 + \frac{\lambda^4(a^2(r^2-8)-r^3)}{a^2(r+2)+\lambda^2 r} + 2a\lambda r^2 + r^5\right)}{r^5\left(-\frac{\lambda^4(r-2)(a^2(r+2)+r^3)}{r^3(a^2(r+2)+\lambda^2 r)} + \frac{2a^2}{r} + a^2 - \frac{4a\lambda}{r} + r^2\right)}\right|_{r_c} \\ &+ \left[\frac{\begin{matrix}2(2a^5\lambda r^2(r+2)^2 + 4a^3\lambda^3 r^3(r+2) + 2a^2\lambda^2 r^3(r+2)(r^3-a^2) + \lambda^6(-r)(r^3-a^2(r^2-8)) \\ +\lambda^4(a^4(r-3)(r+2)^2 - 3a^2r^4 + r^7) + a^4r^2(r+2)^2(r^3-a^2) + 2a\lambda^5 r^4)^2\end{matrix}}{\begin{matrix}r^2(a^2(r+2)+\lambda^2 r)^2(a^4(r+2)^2r^2 - 4a^3\lambda(r+2)r^2 \\ +a^2(r+2)(r^5+\lambda^2r^3-\lambda^4(r-2)) - 4a\lambda^3r^3 + \lambda^2r^6 - \lambda^4(r-2)r^3)^2\end{matrix}}\right]_{r_c}.\end{aligned}$$

Using numerical techniques, Eqs. (16)–(20) may be solved to obtain the phase portrait of the transonic solutions.

C. Flow in hydrostatic equilibrium along the vertical direction

The mass accretion rate is found to be

$$\dot{M}_{VE} = 4\pi\sqrt{\Delta}H(r)\rho\sqrt{\frac{u^2}{1-u^2}}. \tag{21}$$

The disk height can be calculated as

$$H(r) = \sqrt{\frac{2}{\gamma}}r^2\left[\frac{c_s^2(\gamma-1)}{(\gamma-1-c_s^2)F}\right]^{\frac{1}{2}} \tag{22}$$

with $v_t = \sqrt{\frac{f}{1-u^2}}$ and $F = \lambda^2 v_t^2 - a^2(v_t - 1)$. The corresponding entropy accretion rate is given by

$$\dot{\Xi}_{VE} = 4\pi u r^2\left[\frac{c_s^2(\gamma-1)}{\gamma-1-c_s^2}\right]^{\frac{\gamma+1}{2(\gamma-1)}}\left[\frac{2\Delta}{\gamma(1-u^2)F}\right]^{\frac{1}{2}}. \tag{23}$$

The space gradient of c_s and u can be obtained as

$$\frac{dc_s}{dr} = \frac{\mathcal{N}_1^{VE}}{\mathcal{D}_1^{VE}}, \tag{24}$$

$$\frac{du}{dr} = \frac{\mathcal{N}_2^{VE}}{\mathcal{D}_2^{VE}}, \tag{25}$$

where $\mathcal{N}_2^{VE} = \frac{2c_s^2}{\gamma+1}(-\frac{P1 v_t(2\lambda^2 v_t - a^2)}{4F} + \frac{\Delta'}{2\Delta} + \frac{2}{r}) - \frac{P1}{2}$, $\mathcal{D}_2^{VE} = \frac{u}{1-u^2} - \frac{2c_s^2}{\gamma+1}\frac{1}{(1-u^2)u}(1 - \frac{u^2 v_t(2\lambda^2 v_t - a^2)}{2F})$, $P1 = \frac{\Delta'}{\Delta} + \frac{d\Omega}{dr}\frac{\lambda}{1-\Omega\lambda} - \frac{g'_{\phi\phi}+\lambda g'_{t\phi}}{g_{\phi\phi}+\lambda g_{t\phi}}$, and $\Omega = \frac{v^\phi}{v^t}$, where the sub-superscripts VE stand for "vertical equilibrium." This provides the corresponding critical conditions as

$$u^2\Big|_{r_c} = \left.\frac{\mathrm{P1}}{\frac{\Delta'}{\Delta} + \frac{4}{r}}\right|_{r_c}, \tag{26}$$

$$c_s^2\Big|_{r_c} = \left.\frac{(\gamma+1)(2Fu^2)}{2(2F - u^2 v_t(2\lambda^2 v_t - a^2))}\right|_{r_c}. \tag{27}$$

The corresponding space gradients of velocities at critical points are obtained as

$$\left.\frac{du}{dr}\right|_{r_c} = -\frac{\beta_{VE}}{2\alpha_{VE}} \pm \frac{1}{2\alpha_{VE}}\sqrt{\beta_{VE}^2 - 4\alpha_{VE}\Gamma_{VE}}, \tag{28}$$

$$\left.\frac{dc_s}{dr}\right|_{r_c} = \left.\frac{\mathcal{N}_1^{VE}}{\mathcal{D}_1^{VE}}\right|_{r_c}, \tag{29}$$

where the coefficients α_{VE}, β_{VE}, and Γ_{VE} are given by

$$\alpha_{VE}=\frac{1+u^2}{(1-u^2)^2}-\frac{2nD_2D_6}{2n+1},\quad \beta_{VE}=\frac{2nD_2D_7}{2n+1}+\tau_4,$$

$$\Gamma_{VE}=-\tau_3,\quad n=\frac{1}{\gamma-1},\quad D_2=\frac{c_s^2}{u(1-u^2)}(1-D_3),$$

$$D_6=\frac{3u^2-1}{u(1-u^2)}-\frac{D_5}{1-D_3}-\frac{(1-nc_s^2)u}{nc_s^2(1-u^2)},$$

$$D_7=\frac{1-nc_s^2}{nc_s^2}\frac{P1}{2}+\frac{D_3D_4v_tP1}{2(1-D_3)},$$

$$\tau_3=\frac{2n}{2n+1}\left(c_s^2\tau_2-\frac{v_tP1v_1}{2nv_t}(1-nc_s^2)-c_s^2v_5v_t\frac{P1}{2}\right)-\frac{P1'}{2},$$

$$\tau_4=\frac{2n}{2n+1}\frac{v_tu}{1-u^2}\left(\frac{v_1}{nv_t}(1-nc_s^2)+c_s^2v_5\right),$$

$$v_1=\frac{\Delta'}{2\Delta}+\frac{2}{r}-(2\lambda^2v_t-a^2)v_t\frac{\mathrm{P1}}{4F},$$

$$D_3=\frac{u^2v_t(2\lambda^2v_t-a^2)}{2F},\quad D_4=\frac{1}{v_t}+\frac{2\lambda^2}{2\lambda^2v_t-a^2}-\frac{2\lambda^2v_t-a^2}{F},$$

$$D_5=D_3\left(\frac{2}{u}+\frac{D_4v_tu}{1-u^2}\right),\quad \tau_2=\tau_1-\frac{v_t(2\lambda^2v_t-a^2)}{4F}P1',$$

$$v_5=(2\lambda^2v_t-a^2)\frac{P1}{4F}v_4,\quad \tau_1=\frac{1}{2}\left(\frac{\Delta''}{\Delta}-\frac{(\Delta')^2}{\Delta^2}\right)-\frac{2}{r^2},$$

$$v_4=\frac{v_3}{(2\lambda^2v_t-a^2)F},\quad v_3=(4\lambda^2v_t-a^2)F-(2\lambda^2v_t-a^2)^2v_t.$$

Note that the Mach number is not unity at the critical points. Hence, apparently the critical points and the sonic points are not isomorphic. This issue may be resolved in two different ways:

(a) The time-dependent Euler equation and the continuity equation can be linearly perturbed to find the corresponding wave equation which describes the propagation of the acoustic perturbation through the background fluid space-time. The speed of propagation of such a perturbation can be taken as the effective adiabatic sound speed. The critical points become the sonic points for such an effective sound speed. This treatment requires dealing with the time-dependent perturbation techniques, which is beyond the scope of this work. For related calculations, one may refer to Ref. [94], where such a perturbation technique has been applied for accretion in the Schwarzschild metric.

(b) The integral solutions may be numerically carried out starting from the critical point and up to a certain radial distance where the Mach number becomes exactly equal to unity and the corresponding radial distance can be considered the sonic point. In our work, we shall follow this approach.

V. PARAMETER SPACE FOR POLYTROPIC ACCRETION

One obtains [39] the limits for the four parameters governing the flow as $[0<\mathcal{E}<1, 0<\lambda<4, \frac{4}{3}<\gamma<\frac{5}{3}, -1<a<1]$. For polytropic accretion in the Kerr metric, the parameter space is four dimensional. For our convenience, we deal with two-dimensional parameter space. ${}^4C_2$ such spaces may be obtained. For the time being, we concentrate on $[\mathcal{E}-\lambda]$ parameter space for fixed values of $[\gamma, a]$.

Figure 1 shows the $[\mathcal{E}-\lambda]$ parameter space for adiabatic accretion in quasispherical geometry for $[\gamma=1.35, a=0.1]$. Similar diagrams can be produced for the two other geometries as well. $A_1A_2A_3A_4$ represents the region of $[\mathcal{E},\lambda]$ for which the corresponding polynomial equation in r_c along with the corresponding critical point conditions provides three real positive roots lying outside r_+, where $r_+=1+\sqrt{1-a^2}$, with a being the Kerr parameter. For region $A_1A_2A_3$, one finds $\dot{\Xi}_{inner}>\dot{\Xi}_{outer}$, and accretion is multicritical. $A_3A_5A_6$ (shaded in green), which is a subspace of $A_1A_2A_3$, allows shock formation. Such a subspace provides true multitransonic accretion where the stationary transonic solution passing through the outer sonic point joins with the stationary transonic solution constructed through the inner sonic point through a discontinuous energy-preserving shock of Rankine-Hugoniot type. Such a shocked multitransonic solution contains two smooth transonic (from sub to super) transitions at two regular sonic points (of saddle type) and a discontinuous transition (from super to sub) at the shock location.

On the other hand, the region $A_1A_3A_4$ represents the subset of $[\mathcal{E},\lambda,\gamma]_{mc}$ (where the subscript "mc" stands for

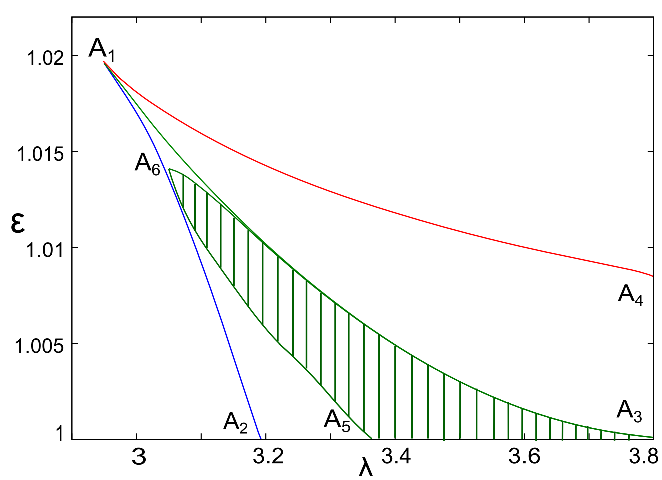

FIG. 1. $\mathcal{E}$-λ plot for quasispherical disk geometry ($\gamma=1.35$ and $a=0.1$).

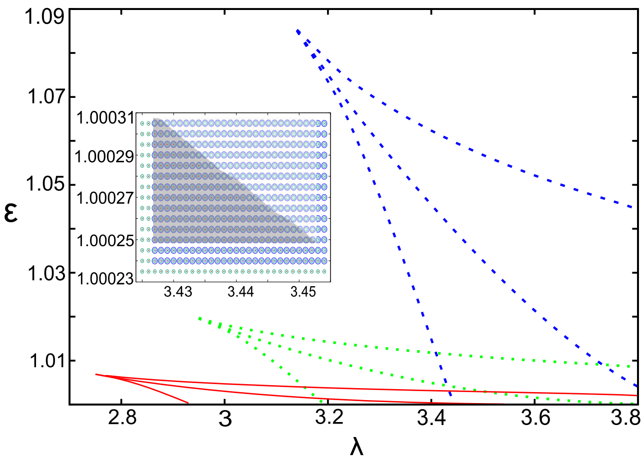

FIG. 2. Comparison of the $\mathcal{E}$-λ plots for three different flow geometries ($\gamma = 1.35$ and $a = 0.1$). Constant height disk, quasi-spherical flow, and flow in vertical hydrostatic equilibrium represented by blue dashed lines, green dotted lines, and red solid lines, respectively. The shaded region in the inset depicts $[\mathcal{E}, \lambda]$ space overlap with multicritical solutions for all three models.

"multicritical"), for which $\dot{\Xi}_{inner} < \dot{\Xi}_{outer}$ and hence incoming flow can have only one critical point of saddle type, and the background flow possesses one acoustic horizon at the inner saddle-type sonic point. The boundary A_1A_3 between these two regions represents the value of $[\mathcal{E}, \lambda, \gamma]$ for which multicritical accretion is characterized by $\dot{\Xi}_{inner} = \dot{\Xi}_{outer}$, and hence the transonic solutions passing through the inner and outer sonic points are completely degenerate, leading to the formation of a heteroclinic orbit [95] on the phase portrait. Such a flow pattern may be subjected to instability and turbulence as well.

In Fig. 2, for the same values of $[\gamma, a]$, we compare the parameter spaces for three different flow geometries. The common region for which multiple critical points are formed for all three flow geometries are shown in the inset.

VI. CLASSIFICATION OF CRITICAL POINTS FOR POLYTROPIC ACCRETION

In the previous section, we found that the transonic accretion may possess, depending on the initial boundary conditions defined by the values of $[\mathcal{E}, \lambda, \gamma, a]$, one or three critical points. Since we consider inviscid, nondissipative flow, the critical points are expected to be either of saddle type or of center type. No spiral- (instead of center-type) or nodal-type points may be observed. The nature of the critical points, whose locations are obtained by substituting the critical point conditions for accretion flow into different geometries and solving for the equation of specific energy, cannot be determined from such solutions. A classification scheme has been developed [90] to accomplish such a task. Once the location of a critical point is identified, the linearized study of the space gradients of the square of the advective velocity in the close neighborhood of such a point may be carried out to develop a complete and rigorous mathematical classification scheme to understand whether a critical point is of saddle type or of center type. Such a methodology is based on a local classification scheme. A global understanding of the flow topology is not possible to accomplish using such a scheme. For that purpose, study of the stationary integral flow solution, which can be accomplished only numerically, is necessary. Such a numerical scheme to obtain the global phase portraits will be discussed in detail in the subsequent sections.

Stationary axisymmetric accretion in the Kerr metric can be described by a first order autonomous differential equation [90] to apply the formalism borrowed from dynamical systems theory and to find out the nature of the critical points using such a formalism. Below, we generalize such an analysis for polytropic accretion in three different models.

A. Constant height flow

The gradient of the square of the sound speed and the dynamical flow velocity (the advective velocity) can be written as

$$\frac{dc_s^2}{dr} = (\gamma - 1 - c_s^2)\left[\frac{-1}{2(1-u^2)}\frac{du^2}{dr} - \frac{f'}{2f}\right], \tag{30}$$

$$\frac{du^2}{dr} = \frac{2[\frac{r-1}{\Delta}c_s^2 - \frac{f'}{2f}]}{\frac{1}{u^2}(\frac{1}{1-u^2})(u^2 - c_s^2)}. \tag{31}$$

One can decompose the expression for $\frac{du^2}{dr}$ into two parametrized equations using a dummy mathematical parameter τ as

$$\frac{du^2}{d\tau} = 2\left[\frac{r-1}{\Delta}c_s^2 - \frac{f'}{2f}\right],$$
$$\frac{dr}{d\tau} = \frac{1}{u^2}\left(\frac{1}{1-u^2}\right)(u^2 - c_s^2). \tag{32}$$

The above equation is an autonomous equation, and hence τ does not explicitly appear on the right-hand sides. About the fixed values of the critical points, one uses a perturbation prescription of the following form,

$$u^2 = u_c^2 + \delta u^2, \tag{33}$$

$$c_s^2 = c_{sc}{}^2 + \delta c_s^2, \tag{34}$$

$$r = r_c + \delta r, \tag{35}$$

and derives a set of two autonomous first order linear differential equations in the $\delta r - \delta u^2$ plane by expressing δc_s^2 in terms of δr and δu^2 as

$$\frac{\delta c_s^2}{c_{sc}^2} = (\gamma - 1 - c_{sc}^2)\left[\frac{-1}{2u_c^2(1-u_c^2)}\delta u^2 - \frac{r_c - 1}{\Delta_c}\delta r\right]. \tag{36}$$

This form of δc_s^2 has been derived using the modified form (in terms of u^2 instead of u) of the mass accretion rate [Eq. (7)] and its corresponding expression for the entropy accretion rate Eq. (8)]. Through this procedure, a set of coupled linear equations in δr and δu^2 will be obtained as

$$\frac{d}{d\tau}(\delta u^2) = \mathcal{A}_{CH}\delta u^2 + \mathcal{B}_{CH}\delta r, \tag{37}$$

$$\frac{d}{d\tau}(\delta r) = \mathcal{C}_{CH}\delta u^2 + \mathcal{D}_{CH}\delta r, \tag{38}$$

where

$$\mathcal{A}_{CH} = \frac{(1-r_c)(\gamma - 1 - c_{s_c}^2)}{\Delta_c(1-u_c^2)}, \tag{39}$$

$$\mathcal{B}_{CH} = 2\left[\frac{c_{s_c}^2}{\Delta_c} - \frac{(r_c-1)^2 c_{s_c}^2}{\Delta_c^2}(\gamma + 1 - c_{s_c}^2) - \frac{f''}{2f} + \frac{1}{2}\left(\frac{f'}{f}\right)^2\right], \tag{40}$$

$$\mathcal{C}_{CH} = \left[1 + \frac{(\gamma - 1 - c_{s_c}^2)}{2(1-u_c^2)}\right]\frac{1}{u_c^2(1-u_c^2)}, \tag{41}$$

$$\mathcal{D}_{CH} = -\mathcal{A}_{CH}. \tag{42}$$

Using trial solutions of the form $\delta u^2 \sim \exp(\Omega\tau)$ and $\delta r \sim \exp(\Omega\tau)$ [Ω, in this context, should not be confused with the angular velocity of the flow in Eq. (5)], the eigenvalues of the stability matrix can be expressed as

$$\Omega_{CH}^2 \equiv \Omega_{CH_1}\Omega_{CH_2} = \mathcal{B}_{CH}\mathcal{C}_{CH} - \mathcal{A}_{CH}\mathcal{D}_{CH}. \tag{43}$$

Once the numerical values corresponding to the location of the critical points are obtained, it is straightforward to calculate the numerical value corresponding to the expression for Ω^2 since Ω^2 is essentially a function of r_c. The accreting black hole system under consideration is a conservative system; hence, either $\Omega^2 > 0$, which implies that the critical points are of saddle type, or one obtains $\Omega^2 < 0$, which implies that the critical points are of center type. One thus understands the nature of the critical points (whether saddle type or center type) once the value of r_c is known. It has been observed that the single critical point solutions are always of saddle type. This is obvious, otherwise monotransonic solutions would not exist. It is also observed that for multicritical flow, the middle critical point is of center type and the inner and the outer critical points are of saddle type. This will be explicitly shown diagrammatically in the subsequent sections.

B. Conical flow

The gradient of the square of the sound speed and the advective velocity are given by

$$\frac{dc_s^2}{dr} = (\gamma - 1 - c_s^2)\left[\frac{-1}{2(1-u^2)}\frac{du^2}{dr} - \frac{f'}{2f}\right], \tag{44}$$

$$\frac{du^2}{dr} = \frac{2\left[\frac{(2r^2-3r+a^2)}{\Delta r}c_s^2 - \frac{f'}{2f}\right]}{\frac{1}{u^2}\left(\frac{1}{1-u^2}\right)(v^2 - c_s^2)}. \tag{45}$$

The parametrized form of the expression of $\frac{du^2}{dr}$ is given by the equations

$$\frac{du^2}{d\tau} = 2\left[\frac{(2r^2-3r+a^2)}{\Delta r}c_s^2 - \frac{f'}{2f}\right],$$
$$\frac{dr}{d\tau} = (u^2 - c_s^2)\frac{1}{u^2(1-u^2)}. \tag{46}$$

Using the perturbation scheme of Eqs. (33)–(35), we obtain

$$\frac{\delta c_s^2}{c_{s_c}^2} = (\gamma - 1 - c_{s_c}^2) \times \left[-\frac{1}{2u_c^2(1-u_c^2)}\delta u^2 - \frac{(2r_c^2 - 3r_c + a^2)}{\Delta_c r_c}\delta r\right], \tag{47}$$

where δc_s^2 has been derived using a modified form of Eqs. (14) and (15). The coupled linear equations in δr and δu^2 are given by

$$\frac{d}{d\tau}(\delta u^2) = \mathcal{A}_{CF}\delta u^2 + \mathcal{B}_{CF}\delta r, \tag{48}$$

$$\frac{d}{d\tau}(\delta r) = \mathcal{C}_{CF}\delta u^2 + \mathcal{D}_{CF}\delta r, \tag{49}$$

where

$$\mathcal{A}_{CF} = -\frac{(2r_c^2 - 3r_c + a^2)(\gamma - 1 - c_{s_c}^2)}{\Delta_c r_c(1-u_c^2)}, \tag{50}$$

$$\mathcal{B}_{CF} = \frac{2(4r_c - 3)c_{s_c}^2}{\Delta_c r_c} - \frac{f''}{f} + \left(\frac{f'}{f}\right)^2 - \frac{2c_{s_c}^2}{\Delta_c^2 r_c^2}(2r_c^2 - 3r_c + a^2) \times [(3r_c^2 - 4r_c + a^2) + (\gamma - 1 - c_{s_c}^2)(2r_c^2 - 3r_c + a^2)], \tag{51}$$

$$\mathcal{C}_{CF} = \left[1 + \frac{(\gamma - 1 - c_{s_c}^2)}{2(1-u_c^2)}\right]\frac{1}{u_c^2(1-u_c^2)}, \tag{52}$$

$$\mathcal{D}_{CF} = -\mathcal{A}_{CF}. \tag{53}$$

Using the prescription mentioned in the previous subsection, eigenvalues of the stability matrix are obtained as

$$\Omega_{CF}^2 \equiv \Omega_{CF_1}\Omega_{CF_2} = \mathcal{B}_{CF}\mathcal{C}_{CF} - \mathcal{A}_{CF}\mathcal{D}_{CF}. \tag{54}$$

C. Flow in hydrostatic equilibrium along the vertical direction

The gradient of the square of the advective velocity is given by

$$\frac{du^2}{dr} = \frac{\beta^2 c_s^2[\frac{F_1'}{F_1} - \frac{1}{F}\frac{\partial F}{\partial r}] - \frac{f'}{f}}{(1-\frac{\beta^2 c_s^2}{u^2})\frac{1}{(1-u^2)} + \frac{\beta^2 c_s^2}{F}(\frac{\partial F}{\partial u^2})}, \tag{55}$$

where $F_1 = \Delta r^4$ and $\beta = \sqrt{\frac{2}{\gamma+1}}$. The parametrized form of the expression of $\frac{du^2}{dr}$ is given by the equations

$$\frac{du^2}{d\tau} = \beta^2 c_s^2\left[\frac{F_1'}{F_1} - \frac{1}{F}\frac{\partial F}{\partial r}\right] - \frac{f'}{f},$$
$$\frac{dr}{d\tau} = \left(1-\frac{\beta^2 c_s^2}{u^2}\right)\frac{1}{(1-u^2)} + \frac{\beta^2 c_s^2}{F}\left(\frac{\partial F}{\partial u^2}\right). \tag{56}$$

Using the perturbation scheme of Eqs. (33)–(35) and modified forms of Eqs. (21) and (23), we obtain

$$\frac{\delta c_s^2}{c_{s_c}^2} = \mathcal{A}\delta u^2 + \mathcal{B}\delta r, \tag{57}$$

where $\mathcal{A} = -\frac{\gamma-1-c_{s_c}^2}{\gamma+1}[\frac{1}{u_c^2(1-u_c^2)} - \frac{1}{F_c}(\frac{\partial F}{\partial u^2})|_c]$, $\mathcal{B} = -\frac{\gamma-1-c_{s_c}^2}{\gamma+1} \times [\frac{F_1'(r_c)}{F_1(r_c)} - \frac{1}{F_c}(\frac{\partial F}{\partial r})|_c]$. The coupled linear equations in δr and δu^2 are given by

$$\begin{aligned}\frac{\mathrm{d}}{\mathrm{d}\tau}(\delta u^2) &= \beta^2 c_{\mathrm{sc}}^2\left[\frac{\mathcal{A}F_1'}{F_1} - \frac{\mathcal{A}\mathcal{C}}{F} + \frac{\mathcal{C}\mathcal{D}}{F^2} - \frac{\Delta_3}{F}\right]\delta u^2 \\ &\quad + \left[\frac{\beta^2 c_{\mathrm{sc}}^2 F_1'}{F_1}\left\{\mathcal{B} + \left(\frac{F_1''}{F_1'} - \frac{F_1'}{F_1}\right)\right\}\right. \\ &\quad \left. - \frac{f'}{f}\left(\frac{f''}{f'} - \frac{f'}{f}\right) - \frac{\beta^2 c_{\mathrm{sc}}^2\mathcal{C}}{F}\left(\mathcal{B} - \frac{\mathcal{C}}{F} + \frac{\Delta_4}{\mathcal{C}}\right)\right]\delta r, \\ \frac{\mathrm{d}}{\mathrm{d}\tau}(\delta r) &= \left[\frac{1}{(1-u_{\mathrm{c}}^2)^2} - \frac{\beta^2 c_{\mathrm{sc}}^2}{u_{\mathrm{c}}^2(1-u_{\mathrm{c}}^2)}\left\{\mathcal{A} + \frac{2u_{\mathrm{c}}^2 - 1}{(1-u_{\mathrm{c}}^2)^2}\right\}\right. \\ &\quad \left. + \frac{\beta^2 c_{\mathrm{sc}}^2\mathcal{D}}{F}\left(\mathcal{A} - \frac{\mathcal{D}}{F} + \frac{\Delta_1}{\mathcal{D}}\right)\right]\delta u^2 \\ &\quad + \left[-\frac{\beta^2 c_{\mathrm{sc}}^2\mathcal{B}}{u_{\mathrm{c}}^2(1-u_{\mathrm{c}}^2)} + \frac{\beta^2 c_{\mathrm{sc}}^2\mathcal{D}}{F}\left(\mathcal{B} - \frac{\mathcal{C}}{F} + \frac{\Delta_2}{\mathcal{D}}\right)\right]\delta r,\end{aligned} \tag{58}$$

where $\mathcal{C} = (\frac{\partial F}{\partial r})|_c$, $\mathcal{D} = (\frac{\partial F}{\partial u^2})|_c$, $\Delta_1 = \frac{\partial}{\partial u^2}(\frac{\partial F}{\partial u^2})|_c$, $\Delta_2 = \frac{\partial}{\partial r}(\frac{\partial F}{\partial u^2})|_c$, $\Delta_3 = \frac{\partial}{\partial u^2}(\frac{\partial F}{\partial r})|_c$, $\Delta_4 = \frac{\partial}{\partial r}(\frac{\partial F}{\partial r})|_c$. Using the prescription mentioned in the previous subsection, eigenvalues of the stability matrix are obtained as

$$\Omega_{VE}^2 = \beta^4 c_{s_c}^4\chi^2 + \xi_1\xi_2, \tag{59}$$

where $\chi = [\frac{F_1'\mathcal{A}}{F_1} - \frac{\mathcal{A}\mathcal{C}}{F} + \frac{\mathcal{C}\mathcal{D}}{F^2} - \frac{\Delta_3}{F}] = [\frac{\mathcal{B}}{u_c^2(1-u_c^2)} - \frac{\mathcal{B}\mathcal{D}}{F} + \frac{\mathcal{C}\mathcal{D}}{F^2} - \frac{\Delta_2}{F}]$, $\xi_1 = \frac{\beta^2 c_{\mathrm{sc}}^2 F_1'}{F_1}[\mathcal{B} + \frac{F_1''}{F_1'} - \frac{F_1'}{F_1}] - \frac{f'}{f}[\frac{f''}{f'} - \frac{f'}{f}] - \frac{\beta^2 c_{\mathrm{sc}}^2\mathcal{C}}{F}[\mathcal{B} - \frac{\mathcal{C}}{F} + \frac{\Delta_4}{\mathcal{C}}]$, and $\xi_2 = \frac{1}{(1-u_c^2)^2} - \frac{\beta^2 c_{\mathrm{sc}}^2}{u_c^2(1-u_c^2)}[\mathcal{A} + \frac{2u_c^2-1}{u_c^2(1-u_c^2)}] + \frac{\beta^2 c_{\mathrm{sc}}^2\mathcal{D}}{F}[\mathcal{A} - \frac{\mathcal{D}}{F} + \frac{\Delta_1}{\mathcal{D}}]$.

VII. DEPENDENCE OF Ω^2 ON FLOW AND SPIN PARAMETERS FOR POLYTROPIC ACCRETION WITH VARIOUS MATTER GEOMETRIES

In the previous section, we derived the explicit analytical expressions for calculating the numerical values of Ω^2 once the locations of the critical points were known. We also argued that the solutions corresponding to multitransonic accretion consist of three critical points—one of center type and the other two of saddle type. In order to represent a real multitransonic flow, the middle critical point is required to be of center type such that the actual physical flow occurs through the inner and outer critical points, which are required to be of saddle type in nature. In terms of the present analytical formalism, Ω^2 corresponding to the inner and outer critical points must assume a positive numerical value, whereas those corresponding to the middle critical points must be negative. Figures 3–5 establish the validity of this requirement.

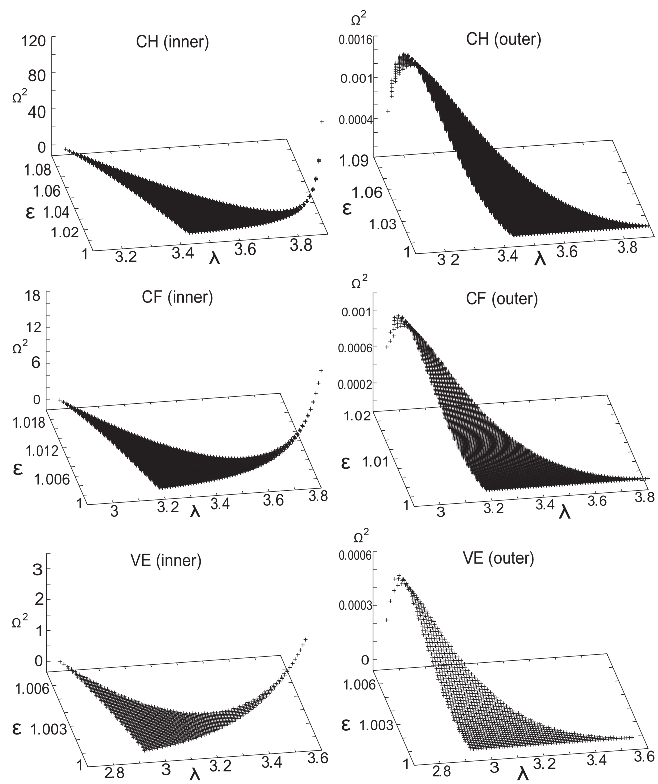

FIG. 3. Comparison of Ω^2 vs $[\mathcal{E}, \lambda]$ of the inner and outer critical points for constant height flow (CH), quasispherical flow (CF), and flow in vertical hydrostatic equilibrium (VE) ($\gamma = 1.35$, $a = 0.1$).

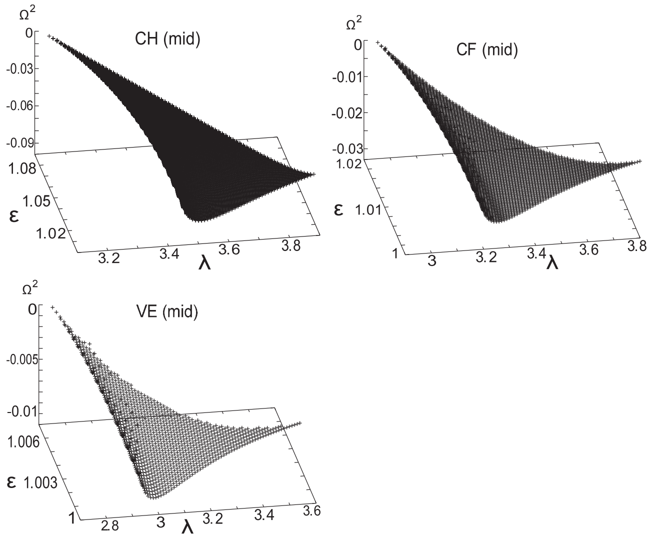

FIG. 4. Comparison of Ω^2 vs $[\mathcal{E}, \lambda]$ of the middle critical point for constant height flow (CH), quasispherical flow (CF), and flow in vertical hydrostatic equilibrium (VE) ($\gamma = 1.35$, $a = 0.1$).

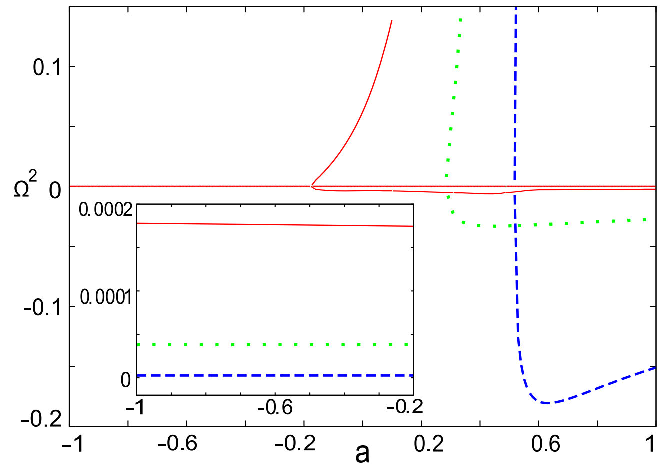

FIG. 5. Comparison of Ω^2 vs a for constant height flow (blue dashed lines), quasispherical flow (green dotted lines), and flow in vertical hydrostatic equilibrium (red solid lines) ($\gamma = 1.35$, $\mathcal{E} = 1.003$, $\lambda = 3.0$). (Inset) Magnified view of the common monotransonic region for the three flow geometries.

In Fig. 3, the variation of Ω^2 for inner and outer critical points has been depicted over the entire physically accessible domain of $[\mathcal{E}, \lambda]$ for a given value of $[\gamma = 1.35, a = 0.1]$. As predicted, the numerical values are all positive, indicating a saddle nature. A similar observation is made in Fig. 4, where the values of Ω^2 for the middle critical points over the entire domain of $[\mathcal{E}, \lambda]$ with the same values of the other flow parameters are negative, indicating a stable point of center type in nature. An immediate comparison can be made between the absolute magnitudes of Ω^2 for the inner and outer critical points. It is interesting to note that $\Omega^2_{inner} \gg \Omega^2_{outer}$, indicating a correlation between the numerical value of the quantity and the influence of gravity due to the central accretor, not only propagated through the value of metric components at the point but also through the dynamical and thermodynamic variables pertaining to the flow. However, it is too far fetched to comment on any physical realization of the quantity at hand, as we are dealing with a highly nonlinear system with a large number of parameters and variables with complicated implicit dependence on one another. It is safe to state only that the sign of the quantity is all that we are interested in at present, to understand the nature of the critical points in order to visualize the phase-space orbits without delving into actual numerics. A comparison of the three different flow geometries reveals that $|\Omega^2|_{CH} > |\Omega^2|_{CF} > |\Omega^2|_{VE}$.

Figure 5 provides an elegant pictorial method of realizing the nature of accretion over the entire range of black hole spin for a given value of specific energy and specific angular momentum of the flow at a particular polytropic index ($\mathcal{E} = 1.003$, $\lambda = 0.3$, $\gamma = 1.35$). The region with a single positive value of Ω^2 (shown in the inset) represents a saddle-type critical point indicating at monotransonic flow for all three geometric configurations. The single positive value is then observed to split into one negative value and two positive values, indicating the formation of one center-type middle critical point and two saddle-type critical points. One of the two saddle points with its numerical value comparable to that of the single saddle-type point in the monotransonic region represents the outer critical point, while the other, with a higher value, represents the inner critical point which is closer to the event horizon. It appears as if a saddle-center pair is generated from the initial saddle at a particular value of spin, and as one moves towards higher values of black hole spin, the new saddle, i.e., the inner critical point moving closer and closer to the horizon begins assuming higher values of Ω^2 until it crosses the horizon and ultimately disappears from the physically accessible regime. And finally, one is left with the center-type middle critical point through which no physical flow can occur, and the previous saddle-type outer critical point through which accretion continues as a purely monotransonic flow. The same universal trend can be observed in all three disk structures, although splitting occurs at different values of a, and the relative magnitudes of Ω^2 are distinct for each flow geometry. It is to be noted that, for the same energy and angular momentum of the accreting fluid, flow in the hydrostatic equilibrium along the vertical direction allows for multitransonic solutions at the lowest values of black hole spin (even for counter-rotating black holes in the given case). It may also be observed that, since the values of Ω^2 represent critical points of a system, the splitting actually corresponds to a *supercritical pitchfork bifurcation* in the theory of dynamical systems where a stable critical point bifurcates into two stable critical points (inner and outer in this case, through which actual flow occurs) and an unstable critical point (middle center-type point through which physical flow in not allowed).

VIII. INTEGRAL FLOW SOLUTIONS WITH SHOCK FOR POLYTROPIC ACCRETION

In the previous section, one finds that it is possible to understand the nature of the critical points through some local stability analysis, i.e., the methodology is applicable in the close neighborhood of the critical points. The global nature of the flow topology, however, is possible to know only through the stationary integral solutions of the corresponding flow equations. Such integral solutions are obtained through numerical techniques. For a particular set of values of $[\mathcal{E}, \lambda, \gamma, a]$, one calculates the location of the critical point(s). The values of $[u, c_s, \frac{du}{dr}, \frac{dc_s}{dr}]$ on such critical points are then computed. Starting from the critical point, the expressions corresponding to $\frac{du}{dr}$ and $\frac{dc_s}{dr}$ are then numerically solved to obtain the radial Mach number vs the radial distance profile. For transonic flow with multiple critical points, a stationary shock may form. For such a flow, integral stationary subsonic solutions pass through the outer sonic point (associated with the saddle-type outer critical point) and becomes supersonic. The supersonic flow then encounters a discontinuous transition through shock and becomes subsonic once again. The location of the shock has to be determined by solving the corresponding shock conditions. The postshock subsonic flow then passes through the inner sonic point (corresponding to the saddle-type inner critical point) to become supersonic again and ultimately plunges into the event horizon.

Figure 6 shows the Mach number vs the radial distance phase portrait of a shocked multitransonic flow for accretion in a quasispherical geometry. Branch AOB (green curve) represents accretion through the outer sonic point O. The flow encounters a stable, standing, energy-preserving shock at $r = r_{sh}^{out}$ whose location is obtained by using the numerical scheme of equating shock-invariant quantities (elaborated in the next subsection). It then jumps along the line of discontinuity BC (blue dashed line). Thus, being transformed into a subsonic, compressed, and hotter flow, it then approaches the event horizon moving along the line $CC'ID$ (red curve) and becoming supersonic once again while passing through the inner sonic point I. $B'C'$ shows an unstable line of discontinuity which is inaccessible to physical flow. FOE represents the corresponding wind solution, while $DIC'CF$ is a homoclinic orbit encompassing the middle critical point M.

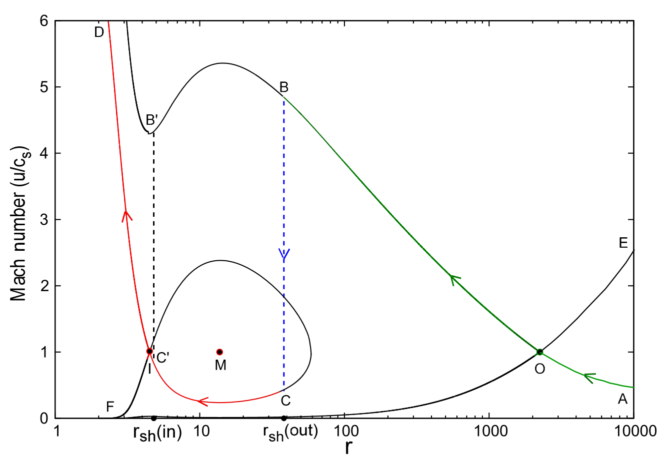

FIG. 6. Phase-space portrait (Mach number vs r plot) for quasispherical disk ($\mathcal{E} = 1.0003$, $\lambda = 3.5$, $\gamma = 1.35$, $a = 0.1$). $r_{sh}^{in} = 4.805$, $r_{sh}^{out} = 38.15$, $r^{in} = 4.5$ (inner sonic point I), $r^{mid} = 13.712$ (middle sonic point M), $r^{out} = 2244.313$ (outer sonic point O).

A. Shock-invariant quantities (S_h)

The *shock-invariant quantity* (S_h) is defined as a quantity whose numerical value remains the same on the integral solution branch passing through the outer sonic point as well as the branch passing through the inner sonic point, exclusively at the location(s) of physically allowed discontinuities obeying the general relativistic Rankine-Hugoniot conditions. Thus, once expression for the shock-invariant quantities are obtained, the corresponding shock locations can be evaluated by numerically checking for the condition $S_h^{out} = S_h^{in}$, where S_h^{out} and S_h^{in} are the shock-invariant quantities defined on the integral flow solutions passing through the outer and the inner sonic points, respectively. The Rankine-Hugoniot conditions applied to a fully general relativistic background flow are given by

$$[[\rho u^\mu]] = 0 \quad \text{and} \quad [[T^{\mu\nu}]] = 0, \tag{60}$$

where $[[V]] = V_- - V_+$, V_+, and V_- symbolically denote the values of some flow variable V before and after the shock, respectively.

Equation (60) can further be decomposed into the following three conditions,

$$[[\rho u^r]] = 0, \tag{61}$$

$$[[(p+\epsilon)u_t u^r]] = 0, \tag{62}$$

$$[[(p+\epsilon)u^r u^r + p]] = 0, \tag{63}$$

where $u^r = \frac{u\Delta^{\frac{1}{2}}}{r\sqrt{1-u^2}}$. Using the definition for specific enthalpy (h) of the fluid given by

$$h = \frac{p+\epsilon}{\rho} \tag{64}$$

and using Eqs. (2) and (4) together with the polytropic equation of state $p = K\rho^\gamma$, one can express ρ, p, and ϵ in terms of the adiabatic sound speed c_s^2 as

$$\rho = \left[\frac{c_s^2(\gamma-1)}{K\gamma(\gamma-1-c_s^2)}\right]^{\frac{1}{\gamma-1}},$$
$$p = K^{\frac{-1}{\gamma-1}}\left[\frac{c_s^2(\gamma-1)}{\gamma(\gamma-1-c_s^2)}\right]^{\frac{\gamma}{\gamma-1}},$$
$$\epsilon = \left(\frac{c_s^2(\gamma-1)}{K\gamma(\gamma-1-c_s^2)}\right)^{\frac{1}{\gamma-1}}\left[1+\frac{1}{\gamma}\left(\frac{c_s^2}{\gamma-1-c_s^2}\right)\right]. \quad (65)$$

Now, considering that the geometry of the flow equation (61) can be rewritten as

$$[[\rho u^r \mathcal{H}(r)]] = 0, \quad (66)$$

where the accretion-geometry-dependent terms $\mathcal{H}(r)$ for three different flow structures are given by

$$\mathcal{H}_{CH}(r) = 2\pi r H,$$
$$\mathcal{H}_{CF}(r) = \Theta r^2,$$
$$\mathcal{H}_{VE}(r) = 4\pi r H(r), \quad (67)$$

with H being the thickness of the constant height disk, Θ being the solid angle subtended by the quasispherical disk at the horizon, and $H(r)$ being the radius-dependent thickness for flow in hydrostatic equilibrium along the vertical direction given by Eq. (22).

Substituting Eqs. (67) and (65) into Eqs. (66) and (63) and then solving simultaneously, we derive the shock-invariant quantities (S_h) for all three flow geometries as

$$S_h|_{CH} = \frac{u^2(\gamma\frac{\Delta}{r^2} - c_s^2) + c_s^2}{u\sqrt{1-u^2}(\gamma-1-c_s^2)}, \quad (68)$$

$$S_h|_{CF} = \frac{u^2(\gamma\frac{\Delta}{r^2} - c_s^2) + c_s^2}{u\sqrt{1-u^2}(\gamma-1-c_s^2)}, \quad (69)$$

$$S_h|_{VE} = \frac{\sqrt{F}\{u^2(\gamma\frac{\Delta}{r^2} - c_s^2) + c_s^2\}}{uc_s\sqrt{(1-u^2)(\gamma-1-c_s^2)}}. \quad (70)$$

IX. SHOCK PARAMETER SPACE FOR POLYTROPIC ACCRETION

We now intend to see which region of the $[\mathcal{E}-\lambda]$ parameter space allows shock formation. For a fixed set of $[\gamma = 1.35,\ a = 0.57]$, we check the validity of the Rankine-Hugoniot condition corresponding to every value of $[\mathcal{E},\lambda]$ for which the accretion flow possesses three critical points. This means that the shock-invariant quantity is calculated for every $[\mathcal{E},\lambda]$ for which the multitransonic accretion is possible, and it is observed that the quantities calculated along the solution passing through the outer and inner sonic points become equal at a particular radial distance, i.e., at the shock location, only for a subset of such $[\mathcal{E},\lambda]$. We then plot the corresponding $[\mathcal{E},\lambda]_{shock}$ for various geometric configurations of matter.

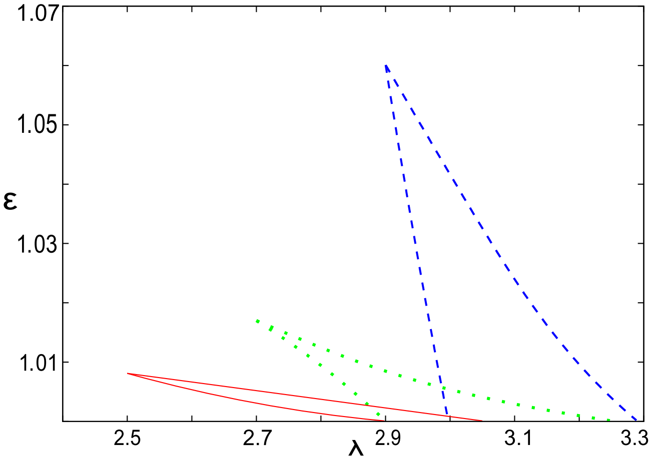

FIG. 7. Comparison of $\mathcal{E}$-λ plots of allowed shocked multitransonic accretion solutions for three different flow geometries ($\gamma = 1.35$ and $a = 0.57$). Constant height disk, quasispherical flow, and flow in vertical hydrostatic equilibrium represented by blue dashed lines, green dotted lines, and red solid lines, respectively.

In Fig. 7, we plot such shock-forming parameter space for three different flow geometries. The shock-forming region of $[\mathcal{E},\lambda]$ for a relevant combination of a and γ, which is common to all three geometries, is shown in Fig. 8. Similarly, Fig. 9 shows the domain of $[a,\lambda]$ for a given value of $\mathcal{E}$ and γ where shock-forming regions of the three flow models overlap. This particular plot indicates at the requirement of an anticorrelation between the angular momentum of flow and spin of the central gravitating source for multitransonic accretion to occur. Moreover, it may be observed that a higher difference between these two values allows for a greater multitransonic shock-forming region. The only probable reason behind this typical

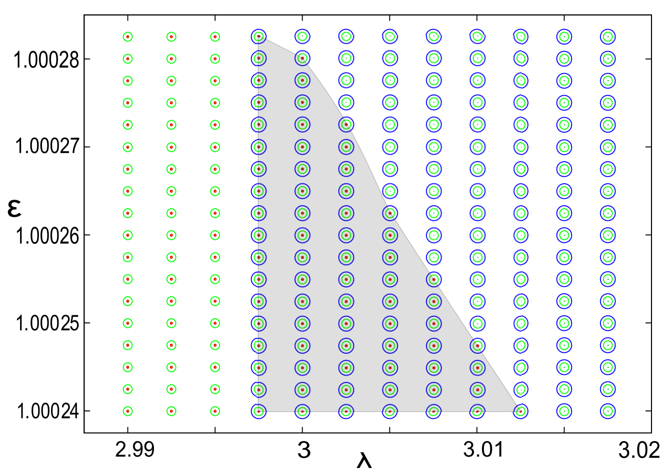

FIG. 8. Shaded region depicts the common domain of $[\mathcal{E},\lambda]$ ($\gamma = 1.35$, $a = 0.57$), which allows shock formation in a constant height disk (blue circles), quasispherical disk (green circles), and flow in hydrostatic equilibrium (red dots).

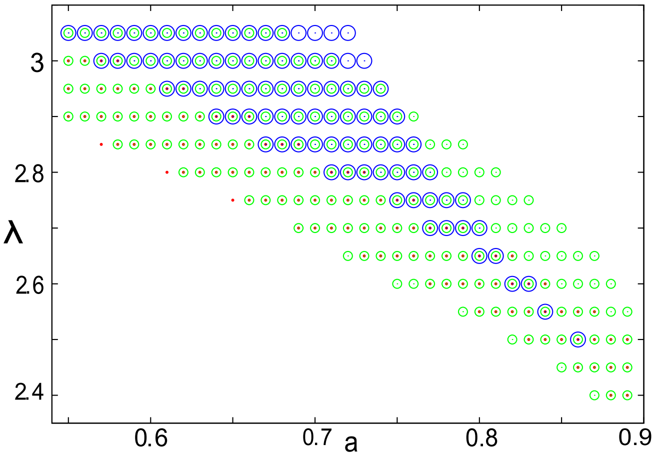

FIG. 9. Overlap region of $[a, \lambda]$ ($\gamma = 1.35$, $\mathcal{E} = 1.00024$), which allows shock formation in a constant height disk (blue circles), quasispherical disk (green circles), and flow in hydrostatic equilibrium (red dots).

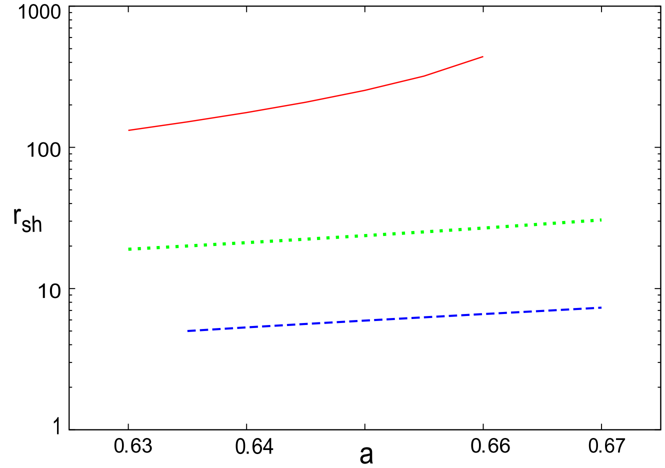

FIG. 10. Shock location (r_{sh}) vs a plot ($\gamma = 1.35$, $\mathcal{E} = 1.00024$, $\lambda = 2.9$) for a constant height disk (dashed blue line), quasispherical disk (dotted green line), and flow in hydrostatic equilibrium (solid red line).

observation seems to be an increase in the effective centrifugal barrier experienced by the flow. These overlapping parameter space domains are of extreme importance for our purposes. All of the shock-related flow properties for which the flow behavior is to be compared for three different geometries are to be characterized by $[\mathcal{E}, \lambda, \gamma, a]$ corresponding to these common regions only. We will show this in greater detail in subsequent sections.

In what follows, we will study the dependence of the shock location (r_{sh}), shock strength (the ratio of pre- to postshock values of the Mach number, M_+/M_-), shock compression ratio (the ratio of the post- to preshock matter density, ρ_-/ρ_+), and the ratio of post- to preshock temperature (T_-/T_+) and pressure (P_-/P_+) on the black hole spin parameter a. The subscripts "+" and "−" represent pre- and postshock quantities, respectively. One can study the dependence of such quantities on other accretion parameters, i.e., $[\mathcal{E}, \lambda, \gamma]$, as well. Such dependence, however, is not very relevant for our study in this work since, for a fixed value of the Kerr parameter, the nature of such dependence should actually be equivalent to the corresponding nature of the dependence of $[r_{sh}, M_+/M_-, \rho_-/\rho_+, P_-/P_+]$ on $[\mathcal{E}, \lambda, \gamma]$, as observed in the Schwarzschild metric which has already been investigated in [92]. Hereafter in this work, we will study the dependence of every physical quantity on the Kerr parameter only for a fixed set of $[\mathcal{E}, \lambda, \gamma]$.

Figure 10 depicts variation of the shock location (r_{sh}) with spin parameter a. The value of λ in this figure and all subsequent figures illustrating other shock-related quantities has been chosen from the common region in Fig. 9 so as to ensure the maximum possible overlapping range of a permissible for shocked accretion at a given value of $\mathcal{E}$ and γ for all three flow models. The shock location is observed to shift further from the horizon as the black hole spin increases. This is what we may expect, as an increasing Kerr parameter for a fixed angular momentum of the flow implies growth in the difference of the two parameters, thus strengthening the effective centrifugal barrier. Thus, transonicity and shock formation are speculated to occur in earlier phases of the flow at greater distances from the massive central source. A comparison of the models reveals the following trend at a given value of a, $r_{sh}(VE) > r_{sh}(CF) > r_{sh}(CH)$. This indicates the fact that flow in hydrostatic equilibrium has to face much more opposition than the other two disk geometries for the same amount of impediment posed by the rotation of the flow and that of the black hole.

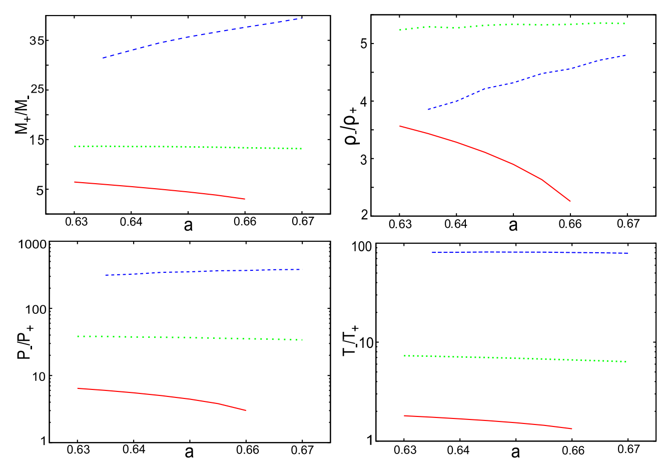

FIG. 11. Variation of shock strength (M_+/M_-), compression ratio (ρ_-/ρ_+), pressure ratio (P_-/P_+), and temperature ratio (T_-/T_+) with black hole spin parameter a ($\gamma = 1.35$, $\mathcal{E} = 1.00024$, $\lambda = 2.9$) for a constant height flow (dashed blue lines), quasispherical flow (dotted green lines), and flow in hydrostatic equilibrium (solid red lines). Subscripts "+" and "−" represent pre- and postshock quantities, respectively.

It is also interesting to note from Fig. 11 that not only does the vertical equilibrium model experience maximum hindrance due to rotation, but it also exhibits the formation of shocks with the weakest strength, i.e., the preshock to postshock ratio of the Mach number (M_+/M_-), when compared with the other two models. The shocks are strongest in the case of disks with a constant height, and intermediate in the case of quasispherical flows. The strengths are observed to decrease with a. This might be explained by the dependence of shock location on the spin parameter. Greater values of r_{sh} point at decreasing curvature of physical space-time leading to diminishing influence of gravity. Thus, dropping of shock strength with increasing a, or, in other words, higher values of r_{sh}, establishes that weaker gravity amounts to the formation of weaker discontinuities in the flow, and vice versa. Naturally, waning shock strengths in turn lead to lower post- to preshock compression (ρ_-/ρ_+), pressure (P_-/P_+), and temperature (T_-/T_+) ratios, as observed in the figure. A seemingly anomalous behavior is observed in this context for the constant height flow geometry, in which case, in spite of an outward shifting of the shock location, shock strength is seen to increase, although the behavior of the other related ratios falls in line with our previous arguments. We shall try to discuss the reason behind such an anomaly in the next section.

X. QUASITERMINAL VALUES

Accreting matter manifests extreme behavior before plunging through the event horizon because it experiences the strong curvature of space-time close to the black hole. The spectral signature of such matter corresponding to that length scale helps to understand the key features of the strong gravity space-time to the close proximity of the horizon. It may also help to study the spectral signature of black hole spin. The corresponding spectral profiles and the light curves may be used for constructing the relevant black hole shadow images [96–101].

For a very small positive value of δ (~0.0001), any accretion variable V_δ measured at a radial distance $r_\delta = r_+ + \delta$ will be termed a "quasiterminal value" of the corresponding accretion variable. In Ref. [39], dependence of V_δ on the Kerr parameter was studied for polytropic accretion flow in hydrostatic equilibrium along the vertical direction. In this work, we intend to generalize such work by computing the V_δ for all three different matter geometries. This generalization will be of paramount importance in understanding the geometric configuration of matter flow close to the horizon through the imaging of the shadow.

In what follows, we will study the dependence of $[M, \rho, T, P]_{r_\delta}$ on the Kerr parameter for shocked multitransonic accretion in three different flow geometries to understand how the nature of such a dependence gets influenced by the flow structure. We will also study such a dependence for monotransonic flows for the entire range of Kerr parameters, going from -1 to $+1$, to study whether any general asymmetry exists between corotating and counterrotating accretion in connection to values of the corresponding V_δ.

A. Dependence of $[M,T,\rho,P]_{r_\delta}$ on a for shocked polytropic accretion

Figure 12 demonstrates how the quasiterminal values pertaining to Mach number (M_δ), density (ρ_δ), pressure (P_δ), and bulk ion temperature (T_δ) vary with black hole spin a, at a given set of $[\mathcal{E}, \lambda, \gamma]$ chosen such that a substantial range of a is available for studying any observable trend of variation in the common shock regime for all three matter configurations. It might be noted that, although a general course of dependence of the values may be observed within a local set of flow parameters for each geometry separately, it is impossible to conclude with any global trends of the sort. This is primarily due to the reason that each permissible set of $[\mathcal{E}, \lambda, \gamma]$ offers an exclusively different domain of black hole spin for multitransonic accretion to occur, and an even narrower common window for the viability of general relativistic Rankine-Hugoniot-type shocks in different geometric configurations of the flow. Hence, in spite of the fact that physical arguments may be able to specifically establish the observed results in certain cases, as it could be done with results obtained in the previous sections, similar specific attempts made in all cases globally may turn out to be not only futile but also dangerously misleading. The anomaly which was pointed out in the preceding section is a stark example of such an instance. However, there is absolutely no reason to disbelieve in the universality or the validity of previous physical arguments. It is only that nature offers a few

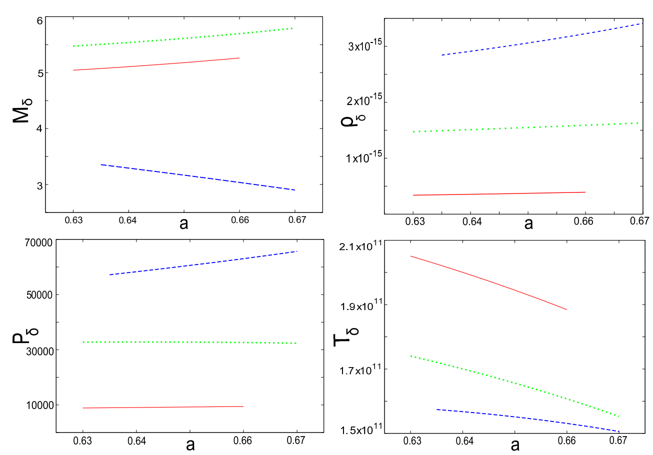

FIG. 12. Variation of quasiterminal values of Mach number (M_δ), density (ρ_δ), pressure (P_δ), and temperature (T_δ) with a ($\gamma = 1.35$, $\mathcal{E} = 1.00024$, $\lambda = 2.9$) for constant height flow (dashed blue lines), quasispherical flow (dotted green lines), and flow in hydrostatic equilibrium (solid red lines). Density and pressure are in centimeter-gram-second (cgs) units of g cm^{-3} and dyn cm^{-2}, respectively, and temperature is in absolute units of kelvin.

select cases to provide us the opportunity of peeking into its global behavior. We present exactly such a case in the following subsection.

B. Dependence of $[M,T,\rho,P]_{r_\delta}$ on a for monotransonic accretion

In Fig. 13, we show the dependence of quasiterminal values on black hole spin for monotransonic accretion. It is observed that weakly rotating and substantially hot flows allow for stationary monotransonic solutions over the entire range of Kerr parameters. From a careful glance at the results, it becomes clear that the reason behind the previously stated anomaly in the general spin-dependent behavior of the corresponding physical quantities for three different flow geometries is essentially due to intrinsic limitations in the possibility of observing their variations over the complete range of spin. Since, for any given set of $[\mathcal{E},\lambda,\gamma]$, shocked stationary multitransonic accretion solutions for all matter configurations are allowed over a considerably small overlapping domain of a, one is able to look only through a narrow slit of the whole window. It is clearly evident from Fig. 13 that the quasiterminal values indeed exhibit common global trends of variation over a for all three geometric configurations. However, while concentrating upon a small portion of spin, asymmetry in the distribution of such trends leads to crossovers and apparently noncorrelative or anticorrelative mutual behaviors among the various flow models. Hence, it is natural to question the utility of results with such constraints at the intrinsic level. But it is this very asymmetry that turns out to be of supreme importance in pointing towards a prospective observational signature of the black hole spin.

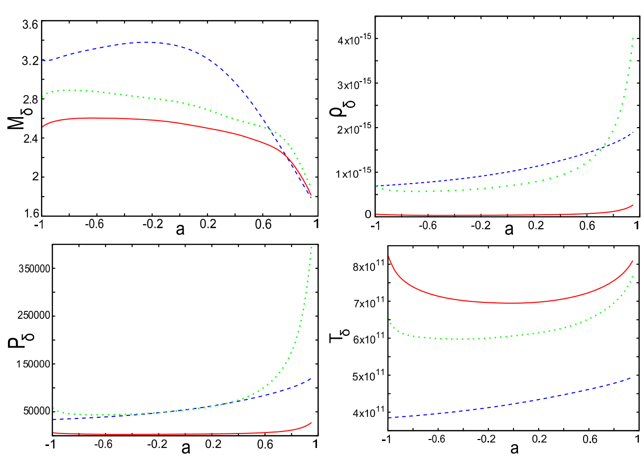

FIG. 13. Variation of quasiterminal values of Mach number (M_δ), density (ρ_δ), pressure (P_δ), and temperature (T_δ) with a ($\gamma = 1.35$, $\mathcal{E} = 1.2$, $\lambda = 2.0$) for monotransonic accretion in constant height flow (dashed blue lines), quasispherical flow (dotted green lines), and flow in hydrostatic equilibrium (solid red lines). Density and pressure are in cgs units of g cm^{-3} and dyn cm^{-2}, respectively, and temperature is in absolute units of kelvin.

XI. ISOTHERMAL FLOW STRUCTURES FOR VARIOUS MATTER GEOMETRIES

The equation of state characterizing isothermal fluid flow is given by

$$p = c_s^2\rho = \frac{\mathcal{R}}{\mu}\rho T = \frac{k_B\rho T}{\mu m_H}, \tag{71}$$

where T is the bulk ion temperature, $\mathcal{R}$ is the universal gas constant, k_B is the Boltzmann constant, m_H is the mass of the hydrogen atom, and μ is the mean molecular mass of fully ionized hydrogen. The temperature T, as introduced in the above equation and which has been used as one of the parameters to describe the isothermal accretion, is the temperature equivalent of the bulk ion flow velocity. That is the reason why the value appears to be high ($10^{10\text{–}11}$ K) in this work. The actual disk temperature is the corresponding electron temperature, which should be on the order of $10^{6\text{–}7}$ K. The electron temperature may be computed from the corresponding ion temperature by incorporating various radiative processes; see, e.g., Ref. [102]. These calculations for our general relativistic model are, however, beyond the scope of this particular work and will be reported elsewhere. For low angular momentum shocked flow under the influence of the Paczyński and Wiita pseudo-Schwarzschild black hole potential [93], such computations have been performed; see, e.g., Ref. [34], as well as Ref. [49].

The energy-momentum conservation equation obtained by setting the 4-divergence (covariant derivative with respect to ν) of Eq. (1) to be zero is

$$p_{,\nu}(g^{\mu\nu} + v^\mu v^\nu) + (p+\epsilon)v^\nu v^\mu_{;\nu} = 0. \tag{72}$$

Using Eq. (71), the general relativistic Euler equation for isothermal flow becomes

$$\frac{c_s^2}{\rho}\rho_{,\nu}(g^{\mu\nu} + v^\mu v^\nu) + v^\nu v^\mu_{;\nu} = 0. \tag{73}$$

Using the irrotationality condition $\omega_{\mu\nu} = 0$, where $\omega_{\mu\nu} = l^\lambda_\mu l^\sigma_\nu v_{[\lambda;\sigma]}$, with $\omega_{\mu\nu}$ being the vorticity of the fluid, l^λ_μ being the projection operator in the normal direction of v^μ, $l^\lambda_\mu = \delta^\lambda_\mu + v^\lambda v_\mu$, and $v_{[\lambda;\sigma]} = \frac{1}{2}(v_{\sigma;\lambda} - v_{\lambda;\sigma})$, we obtain

$$\partial_\nu(v_\mu\rho^{c_s^2}) - \partial_\mu(v_\nu\rho^{c_s^2}) = 0. \tag{74}$$

Taking the time component, we thus observe that, for an irrotational isothermal flow, $v_t\rho^{c_s^2}$ turns out to be a conserved quantity. The square of this quantity is defined as the *quasispecific energy* given by

$$\xi = v_t^2\rho^{2c_s^2}, \tag{75}$$

where ξ is the first integral of motion for the isothermal flows. The second integral of motion is $\dot{M}$, which is a function of the disk height H. The critical point conditions and expressions for the velocity gradients are computed using the same formalism as illustrated in the case of polytropic flow for three different configurations of the disk geometry.

A. Constant height flow

The radial gradient of the advective velocity is

$$\frac{du}{dr}\bigg|_{CH} = \frac{\frac{1-c_s^2}{2c_s^2}\frac{\Delta'}{\Delta} - \frac{1}{2c_s^2}\frac{B'}{B}}{\frac{1}{u} - \frac{u}{1-u^2}\frac{1-c_s^2}{c_s^2}}. \tag{76}$$

The critical point conditions are

$$u_c^2|_{CH} = c_{sc}{}^2|_{CH} = 1 - \frac{B'}{B}\frac{\Delta}{\Delta'}. \tag{77}$$

The velocity gradient at critical points is

$$\left(\frac{du}{dr}\right)_c\bigg|_{CH} = -\sqrt{\frac{\beta_{CH}}{\Gamma_{CH}}}, \tag{78}$$

where

$$\Gamma_{CH} = \frac{2}{c_{sc}{}^2(1-c_{sc}{}^2)},$$

$$\beta_{CH} = \beta_{CH}^{(1)} + \beta_{CH}^{(2)} + \beta_{CH}^{(3)} - \beta_{CH}^{(4)} - \beta_{CH}^{(5)},$$

$$\beta_{CH}^{(1)} = \frac{2(1-c_{sc}{}^2)(1-r_c)^2}{c_{sc}{}^2(c_{sc}{}^2 + r_c(r_c-2))^2},$$

$$\beta_{CH}^{(2)} = \frac{c_{sc}{}^2 - 1}{c_{sc}{}^2(c_{sc}{}^2 + r_c(r_c-2))},$$

$$\beta_{CH}^{(3)} = \frac{\beta_{CH}^{(31)}}{r_c^4 c_{sc}{}^2(c_{sc}{}^2 + \frac{2c_{sc}{}^2}{r_c} + r_c^2 - \frac{4c_{sc}\lambda}{r_c} - \frac{(r_c-2)(r_c^3 + c_{sc}{}^2(r_c+2))\lambda^4}{r_c^3(c_{sc}{}^2(r_c+2)+r_c\lambda^2)})},$$

$$\begin{aligned}\beta_{CH}^{(31)} = {}& -2c_{sc}{}^2 r_c + 5r_c^4 + 4c_{sc}r_c\lambda + \frac{2c_{sc}{}^2(r_c-2)(r_c^3 + c_{sc}{}^2(r_c+2))\lambda^4(c_{sc}{}^2+\lambda^2)}{(c_{sc}{}^2(r_c+2)+r_c\lambda^2)^3} - \frac{c_{sc}{}^2(r_c-2)(c_{sc}{}^2+3r_c^2)\lambda^4}{(c_{sc}{}^2(r_c+2)+r_c\lambda^2)^2} \\ & - \frac{c_{sc}{}^2(r_c^3 + c_{sc}{}^2(r_c+2))\lambda^4}{(c_{sc}{}^2(r_c+2)+r_c\lambda^2)^2} + \frac{(r_c^3 - c_{sc}{}^2(r_c^2-8))\lambda^4(c_{sc}{}^2+\lambda^2)}{(c_{sc}{}^2(r_c+2)+r_c\lambda^2)^2} + \frac{(2c_{sc}{}^2 - 3r_c)r_c\lambda^4}{c_{sc}{}^2(r_c+2)+r_c\lambda^2},\end{aligned}$$

$$\beta_{CH}^{(4)} = \frac{4(-c_{sc}{}^2 r_c^2 + r_c^5 + 2c_{sc}r_c^2\lambda - \frac{c_{sc}{}^2(r_c-2)(r_c^3+c_{sc}{}^2(r_c+2))\lambda^4}{(c_{sc}{}^2(r_c+2)+r_c\lambda^2)^2} + \frac{(-r_c^3 + c_{sc}{}^2(r_c^2-8))\lambda^4}{c_{sc}{}^2(r_c+2)+r_c\lambda^2})}{c_{sc}{}^2 r_c^5(c_{sc}{}^2 + \frac{2c_{sc}{}^2}{r_c} + r_c^2 - \frac{4c_{sc}\lambda}{r_c} - \frac{(r_c-2)(r_c^3+c_{sc}{}^2(r_c+2))\lambda^4}{r_c^3(c_{sc}{}^2(r_c+2)+r_c\lambda^2)})},$$

$$\beta_{CH}^{(5)} = \frac{\beta_{CH}^{(51)}}{\beta_{CH}^{(52)}},$$

$$\begin{aligned}\beta_{CH}^{(51)} = {}& 2[-c_{sc}{}^6 r_c^2(r_c+2)^2 + 2c_{sc}r_c^4\lambda^5 + 2c_{sc}{}^5 r_c^2(r_c+2)^2\lambda + 4c_{sc}{}^3 r_c^3(r_c+2)\lambda^3 + r_c^4\lambda^4(r_c^3-\lambda^2) \\ & + c_{sc}{}^2 r_c\lambda^2(4r_c^5 + 2r_c^6 - 3r_c^3\lambda^2 - 8\lambda^4 + r_c^2\lambda^4) + c_{sc}{}^4(r_c+2)(2r_c^5 + r_c^6 - 2r_c^3\lambda^2 - 6\lambda^4 - r_c\lambda^4 + r_c^2\lambda^4)]^2,\end{aligned}$$

$$\begin{aligned}\beta_{CH}^{(52)} = {}& [c_{sc}{}^2 r_c^2(c_{sc}{}^2(r_c+2) + r_c\lambda^2)^2][c_{sc}{}^4 r_c^2(r_c+2)^2 - 4c_{sc}{}^3 r_c^2(r_c+2)\lambda - 4c_{sc}r_c^3\lambda^3 + r_c^3\lambda^2(r_c^3 - (r_c-2)\lambda^2) \\ & + c_{sc}{}^2(r_c+2)(r_c^5 + r_c^3\lambda^2 - (r_c-2)\lambda^4)]^2.\end{aligned}$$

Equation (76) can be integrated numerically using Eqs. (77) and (78) to obtain the exact topology of the flow in the phase space.

B. Conical flow

The radial gradient of the advective velocity is

$$\frac{du}{dr}\bigg|_{CF} = \frac{\frac{1-c_s^2}{2c_s^2}\frac{\Delta'}{\Delta} - \frac{1}{2c_s^2}\frac{B'}{B} - \frac{1}{r}}{\frac{1}{u} - \frac{u}{1-u^2}\frac{1-c_s^2}{c_s^2}}. \tag{79}$$

The critical point conditions are

$$u_c^2|_{CF} = c_{sc}{}^2|_{CF} = \frac{\frac{\Delta'}{\Delta} - \frac{B'}{B}}{\frac{2}{r} + \frac{\Delta'}{\Delta}}. \tag{80}$$

The velocity gradient at critical points is

$$\left(\frac{du}{dr}\right)_c\bigg|_{CF} = -\sqrt{\frac{\beta_{CF}}{\Gamma_{CF}}}, \tag{81}$$

where

$$\Gamma_{CF} = \frac{2}{c_{sc}^2(1-c_{sc}^2)},$$
$$\beta_{CF} = \beta_{CF}^{(0)} + \beta_{CF}^{(1)} + \beta_{CF}^{(2)} + \beta_{CF}^{(3)} - \beta_{CF}^{(4)} - \beta_{CF}^{(5)},$$
$$\beta_{CF}^{(0)} = -\frac{1}{r_c^2},$$
$$\beta_{CF}^{(1)} = \frac{2(1-c_{sc}^2)(1-r_c)^2}{c_{sc}^2(c_{sc}^2+r_c(r_c-2))^2},$$
$$\beta_{CF}^{(2)} = \frac{c_{sc}^2-1}{c_{sc}^2(c_{sc}^2+r_c(r_c-2))},$$
$$\beta_{CF}^{(3)} = \frac{\beta_{CF}^{(31)}}{r_c^4 c_{sc}^2(c_{sc}^2+\frac{2c_{sc}^2}{r_c}+r_c^2-\frac{4c_{sc}\lambda}{r_c}-\frac{(r_c-2)(r_c^3+c_{sc}^2(r_c+2))\lambda^4}{r_c^3(c_{sc}^2(r_c+2)+r_c\lambda^2)})},$$
$$\beta_{CF}^{(31)} = -2c_{sc}^2 r_c + 5r_c^4 + 4c_{sc}r_c\lambda + \frac{2c_{sc}^2(r_c-2)(r_c^3+c_{sc}^2(r_c+2))\lambda^4(c_{sc}^2+\lambda^2)}{(c_{sc}^2(r_c+2)+r_c\lambda^2)^3} - \frac{c_{sc}^2(r_c-2)(c_{sc}^2+3r_c^2)\lambda^4}{(c_{sc}^2(r_c+2)+r_c\lambda^2)^2}$$
$$- \frac{c_{sc}^2(r_c^3+c_{sc}^2(r_c+2))\lambda^4}{(c_{sc}^2(r_c+2)+r_c\lambda^2)^2} + \frac{(r_c^3-c_{sc}^2(r_c^2-8))\lambda^4(c_{sc}^2+\lambda^2)}{(c_{sc}^2(r_c+2)+r_c\lambda^2)^2} + \frac{(2c_{sc}^2-3r_c)r_c\lambda^4}{c_{sc}^2(r_c+2)+r_c\lambda^2},$$
$$\beta_{CF}^{(4)} = \frac{4(-c_{sc}^2r_c^2+r_c^5+2c_{sc}r_c^2\lambda-\frac{c_{sc}^2(r_c-2)(r_c^3+c_{sc}^2(r_c+2))\lambda^4}{(c_{sc}^2(r_c+2)+r_c\lambda^2)^2}+\frac{(-r_c^3+c_{sc}^2(r_c^2-8))\lambda^4}{c_{sc}^2(r_c+2)+r_c\lambda^2})}{c_{sc}^2r_c^5(c_{sc}^2+\frac{2c_{sc}^2}{r_c}+r_c^2-\frac{4c_{sc}\lambda}{r_c}-\frac{(r_c-2)(r_c^3+c_{sc}^2(r_c+2))\lambda^4}{r_c^3(c_{sc}^2(r_c+2)+r_c\lambda^2)})},$$
$$\beta_{CF}^{(5)} = \frac{\beta_{CF}^{(51)}}{\beta_{CF}^{(52)}},$$
$$\beta_{CF}^{(51)} = 2[-c_{sc}^6r_c^2(r_c+2)^2+2c_{sc}r_c^4\lambda^5+2c_{sc}^5r_c^2(r_c+2)^2\lambda+4c_{sc}^3r_c^3(r_c+2)\lambda^3+r_c^4\lambda^4(r_c^3-\lambda^2)$$
$$+c_{sc}^2r_c\lambda^2(4r_c^5+2r_c^6-3r_c^3\lambda^2-8\lambda^4+r_c^2\lambda^4)+c_{sc}^4(r_c+2)(2r_c^5+r_c^6-2r_c^3\lambda^2-6\lambda^4-r_c\lambda^4+r_c^2\lambda^4)]^2,$$
$$\beta_{CF}^{(52)} = [c_{sc}^2r_c^2(c_{sc}^2(r_c+2)+r_c\lambda^2)^2][c_{sc}^4r_c^2(r_c+2)^2-4c_{sc}^3r_c^2(r_c+2)\lambda-4c_{sc}r_c^3\lambda^3+r_c^3\lambda^2(r_c^3-(r_c-2)\lambda^2)$$
$$+c_{sc}^2(r_c+2)(r_c^5+r_c^3\lambda^2-(r_c-2)\lambda^4)]^2.$$

The flow profile is then obtained by integrating the velocity gradient using critical point conditions and values of velocity gradients evaluated at the critical points.

C. Flow in vertical hydrostatic equilibrium

The general equation for the height of an accretion disk held by hydrostatic equilibrium in the vertical direction is given by [88]

$$-\frac{2p}{\rho} + \left(\frac{H}{r}\right)^2 \frac{F}{r^2} = 0, \tag{82}$$

where $F = \lambda^2 u_t^2 - a^2(u_t - 1)$. The equation had been derived for flow in the Kerr metric and holds for any general equation of state of the infalling matter. Hence, for isothermal flows, the disk height can be calculated as

$$H = \left[\frac{2c_s^2 r^4}{F}\right]^{\frac{1}{2}}, \tag{83}$$

leading to the following results.

The radial gradient of the advective velocity is

$$\left.\frac{du}{dr}\right|_{VE} = \frac{c_{sc}^2(\frac{\Delta'}{2\Delta}+\frac{2}{r}-(2\lambda^2 v_t - a^2)\frac{v_t P1}{4F}) - \frac{P1}{2}}{\frac{u}{1-u^2} - \frac{c_{sc}^2}{u(1-u^2)}(1-(2\lambda^2 v_t - a^2)\frac{u^2 v_t}{2F})}. \tag{84}$$

The critical point conditions are

$$u_c^2|_{VE} = \frac{P1}{\frac{\Delta'}{\Delta}+\frac{4}{r}}, \tag{85}$$

$$c_{sc}^2|_{VE} = \frac{u_c^2}{1-\frac{u_c^2 v_t(2\lambda^2 v_t - a^2)}{2F}}. \tag{86}$$

The velocity gradient at the critical points is

$$\left.\left(\frac{du}{dr}\right)_c\right|_{VE} = -\frac{\beta_{VE}}{2\alpha_{VE}} \pm \frac{1}{2\alpha_{VE}}\sqrt{\beta_{VE}^2 - 4\alpha_{VE}\Gamma_{VE}}, \tag{87}$$

where

$$\alpha_{VE}=\frac{1+u_c^2}{(1-u_c^2)^2}-D_2D_6,\quad \beta_{VE}=D_2D_7+\tau_4,\quad \Gamma_{VE}=-\tau_3,$$

$$D_2=\frac{c_s^2}{u(1-u^2)}(1-D_3),\quad D_6=\frac{3u^2-1}{u(1-u^2)}-\frac{D_5}{1-D_3},$$

$$D_7=\frac{D_3D_4v_tP1}{2(1-D_3)},\quad \tau_3=\left(c_s^2\tau_2-c_s^2v_5v_t\frac{P1}{2}\right)-\frac{P1'}{2},$$

$$\tau_4=\frac{c_s^2v_5v_tu}{1-u^2},\quad v_1=\frac{\Delta'}{2\Delta}+\frac{2}{r}-(2\lambda^2v_t-a^2)v_t\frac{P1}{4F},$$

$$D_3=\frac{u^2v_t(2\lambda^2v_t-a^2)}{2F},\quad D_4=\frac{1}{v_t}+\frac{2\lambda^2}{2\lambda^2v_t-a^2}-\frac{2\lambda^2v_t-a^2}{F},$$

$$D_5=D_3\left(\frac{2}{u}+\frac{D_4v_tu}{1-u^2}\right),\quad \tau_2=\tau_1-\frac{v_t(2\lambda^2v_t-a^2)}{4F}P1',$$

$$v_5=(2\lambda^2v_t-a^2)\frac{P1}{4F}v_4,\quad \tau_1=\frac{1}{2}\left(\frac{\Delta''}{\Delta}-\frac{(\Delta')^2}{\Delta^2}\right)-\frac{2}{r^2},$$

$$v_4=\frac{v_3}{(2\lambda^2v_t-a^2)F},\quad v_3=(4\lambda^2v_t-a^2)F-(2\lambda^2v_t-a^2)^2v_t.$$

Equation (84) is integrated numerically using Eqs. (86) and (87) to obtain the flow profile and also to locate the sonic points corresponding to the respective critical points.

XII. PARAMETER SPACE FOR ISOTHERMAL ACCRETION

Since the parameter space is three dimensional in the case of isothermal accretion in the Kerr metric, for convenience, we deal with a two-dimensional parameter space among ${}^3C_2$ such possible combinations. The limits for two of the parameters governing the flow are $[0<\lambda<4, -1<a<1]$. For the time being, we concentrate on $[T-\lambda]$ parameter space for a fixed value of a. A general $[T-\lambda]$ diagram for a given accretion disk geometry would look similar to the generic diagram for polytopic accretion shown in Fig. 1.

In Fig. 14, for $a=0.1$, we compare the parameter spaces for three different flow geometries. The common domain for which multiple critical points are formed for all three flow geometries is shown as a shaded region.

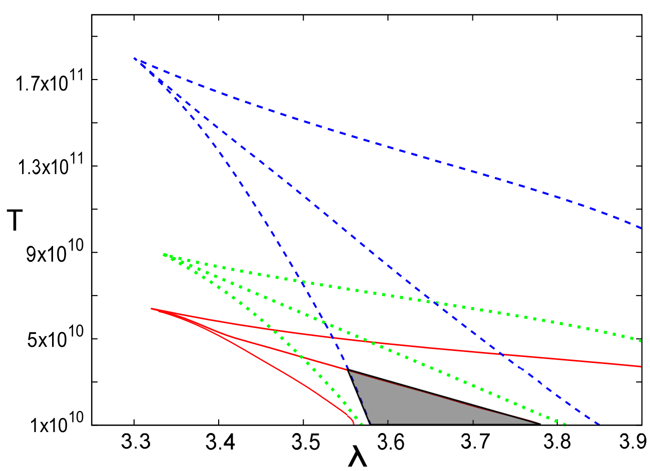

FIG. 14. Comparison of $T-\lambda$ plots for three different flow geometries ($a=0.1$, T in kelvins). Constant height disk, quasi-spherical flow, and flow in vertical hydrostatic equilibrium represented by blue dashed lines, green dotted lines, and red solid lines, respectively. The shaded region allows for multi-critical solutions in all flow configurations.

XIII. CLASSIFICATION OF CRITICAL POINTS FOR ISOTHERMAL ACCRETION

Using the same technique elaborated on in Sec. IV, eigenvalues of the stability matrices for isothermal accretion can be computed for the three disk geometries.

A. Constant height flow

We have

$$\Omega_{CH}^{iso\,2}=\mathcal{B}_{CH}^{iso}\mathcal{C}_{CH}^{iso},\tag{88}$$

where

$$\mathcal{B}_{CH}^{iso}=\frac{f_c'}{f_c}\frac{a^2-1-(r_c-1)^2}{\Delta(r_c-1)}-\frac{f_c''}{f_c}+\left(\frac{f_c'}{f_c}\right)^2,\tag{89}$$

$$\mathcal{C}_{CH}^{iso}=\frac{1}{u_c^2(1-u_c^2)}.\tag{90}$$

B. Conical flow

We have

$$\Omega_{CF}^{iso\,2}=\mathcal{B}_{CF}^{iso}\mathcal{C}_{CF}^{iso},\tag{91}$$

where

$$\mathcal{B}_{CF}^{iso}=\frac{f_c'}{f_c(2r_c^2-3r_c+a^2)}\left(-\frac{\Delta_c}{r_c}+\frac{r_c}{\Delta_c}(a^2-1-(r_c-1)^2)\right)-\frac{f_c''}{f_c}+\left(\frac{f_c'}{f_c}\right)^2,\tag{92}$$

$$\mathcal{C}_{CF}^{iso}=\frac{1}{u_c^2(1-u_c^2)}.\tag{93}$$

C. Flow in hydrostatic equilibrium along the vertical direction

We have

$$\Omega_{VE}^{iso\,2}=\mathcal{B}_{VE}^{iso}\mathcal{C}_{VE}^{iso}-\mathcal{A}_{VE}^{iso}\mathcal{D}_{VE}^{iso},\tag{94}$$

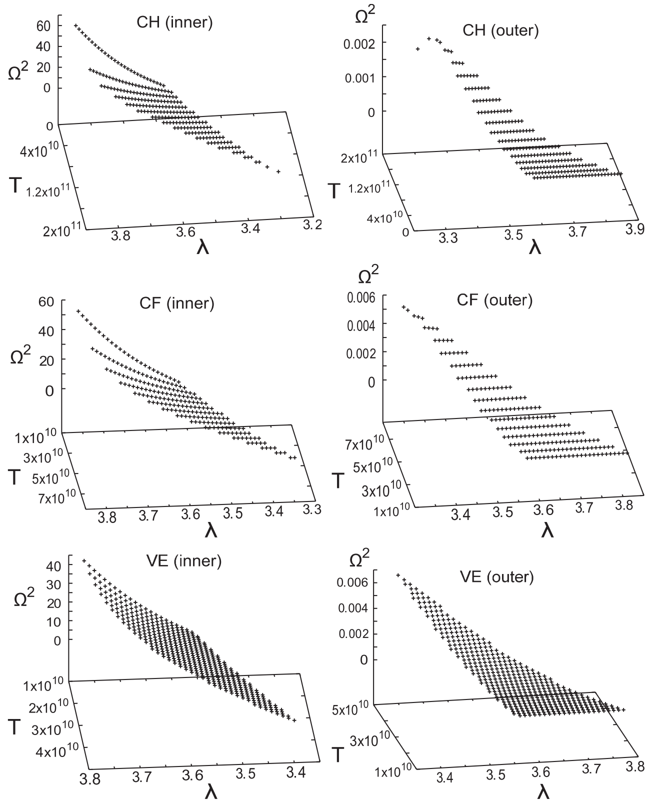

FIG. 15. Comparison of Ω^2 vs $[T, \lambda]$ of the inner and outer critical points for constant height flow (CH), quasispherical flow (CF), and flow in vertical hydrostatic equilibrium (VE) ($a = 0.1$). The left and right panels depict Ω^2 for the inner and outer critical points, respectively, for CH, CF, and VE from top to bottom in the respective order.

$$\mathcal{A}_{VE}^{iso} = \frac{{c_{sc}}^2}{g_2}\left(\frac{(2\lambda^2 v_t - a^2) f_c' g_2'}{2 g_2 \sqrt{(1-u_c^2) f_c}} - \delta_3\right), \tag{95}$$

$$\mathcal{B}_{VE}^{iso} = {c_{sc}}^2 \left(\frac{2}{\Delta_c} - \frac{4}{r_c^2} - \frac{4(r_c-1)^2}{\Delta_c^2} - \frac{\delta_4}{g_2} + \left(\frac{(2\lambda^2 v_t - a^2) f_c'}{2 g_2 \sqrt{(1-u_c^2) f_c}}\right)^2\right) - \frac{f_c''}{f_c} + \left(\frac{f_c'}{f_c}\right)^2, \tag{96}$$

$$\mathcal{C}_{VE}^{iso} = \frac{u_c^4 - 2{c_{sc}}^2 u_c^2 + {c_{sc}}^2}{u_c^4 (1-u_c^2)^2} + \frac{{c_{sc}}^2 \delta_1}{g_2} - \frac{{c_{sc}}^2 g_2'^2}{g_2^2}, \tag{97}$$

$$\mathcal{D}_{VE}^{iso} = -\mathcal{A}_{VE}^{iso}, \tag{98}$$

where $g_2 = (\lambda v_t)^2 - v_t a^2 + a^2$, $\delta_1 = \frac{2\lambda^2 f}{(1-u_c^2)^3} - \frac{3a^2}{4}\sqrt{\frac{f}{(1-u_c^2)^5}}$, $\delta_3 = \frac{\lambda^2 f'}{(1-u_c^2)^2} - \frac{a^2 f'}{4\sqrt{f(1-u_c^2)^3}}$, $\delta_4 = \frac{\lambda^2 f''}{1-u_c^2} - \frac{a^2}{4\sqrt{1-u_c^2}} \frac{2 f f'' - f'^2}{f^{\frac{3}{2}}}$.

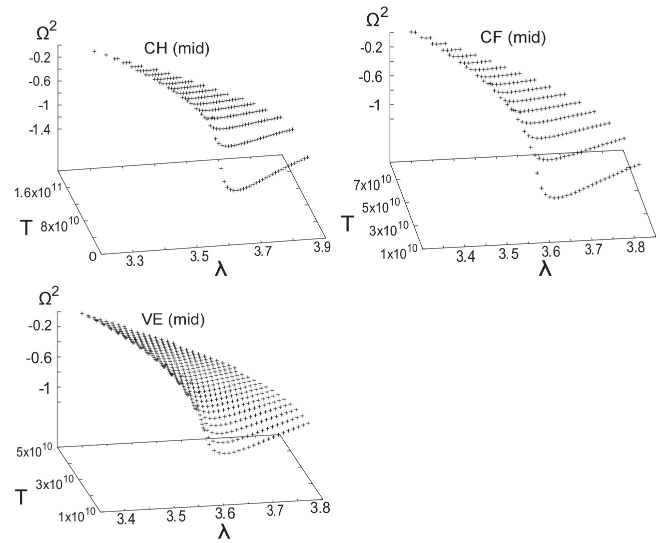

FIG. 16. Comparison of Ω^2 vs $[T, \lambda]$ of the middle critical point for (top left) constant height flow (CH), (top right) quasispherical flow (CF), and (bottom left) flow in vertical hydrostatic equilibrium (VE) ($a = 0.1$).

XIV. DEPENDENCE OF Ω^2 ON FLOW AND SPIN PARAMETERS FOR ISOTHERMAL ACCRETION IN VARIOUS MATTER GEOMETRIES

Figures 15–17, obtained by evaluating the analytical expressions for isothermal flow derived in the previous section at r_c, establish the same argument about multi-transonicity and nature of the critical points as presented in the corresponding section for polytropic flows. The numerical value of Ω^2 assumes a positive sign for the inner and outer saddle-type critical points, and a negative sign for the middle center-type critical points.

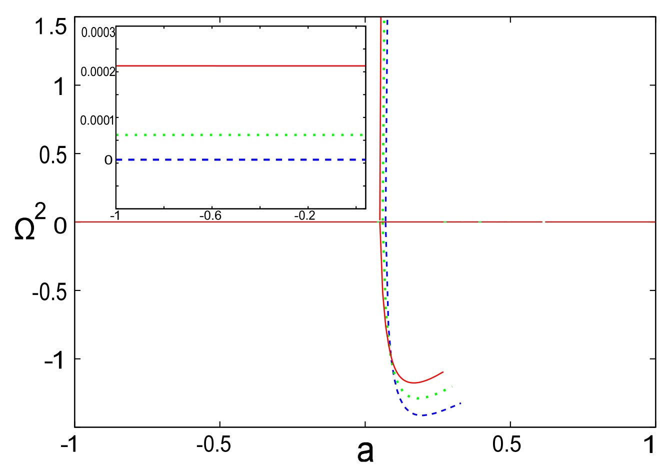

FIG. 17. Comparison of Ω^2 vs a for constant height flow (blue dashed lines), quasispherical flow (green dotted lines), and flow in vertical hydrostatic equilibrium (red solid lines) ($T = 10^{10}$ K, $\lambda = 3.6$). (Inset) Magnified view of the common monotransonic region for the three flow geometries.

In Fig. 15, the variation of Ω^2 for the inner and outer critical points has been depicted over the entire physical domain of $[T, \lambda]$ for a given value of $a = 0.1$. Positive values indicate critical points of a saddle nature. Figure 16 depicts the values of Ω^2 for the middle critical points over the full accessible domain of $[T, \lambda]$ for the same value of a. Negative values indicate critical points which are center type. The same trend of comparison is observed between the absolute magnitudes of Ω^2 for the saddle-type critical points in the case of isothermal flow as well. $\Omega^2_{inner} \gg \Omega^2_{outer}$ once again points towards a correlation between the absolute value of Ω^2 and space-time curvature at the critical points. A comparison of the three different flow geometries reveals that, for inner and middle critical points, $|\Omega^2|_{CH} > |\Omega^2|_{CF} > |\Omega^2|_{VE}$, whereas for the outer critical point, $|\Omega^2|_{VE} > |\Omega^2|_{CF} > |\Omega^2|_{CH}$.

Figure 17 is a similar plot as was obtained for polytropic flow depicting the bifurcation of Ω^2 along black hole spin parameter a for a given value of temperature and a specific angular momentum ($T = 10^{10}$ K, $\lambda = 3.6$). Monotransonic flow through a saddle-type critical point is shown in the inset, where Ω^2 assumes a single positive value for all three flow geometries. The monotransonic flow then bifurcates into multitransonic flow with a center-type middle critical point (with negative value), a saddle-type inner critical point (with a larger positive value), and a saddle-type outer critical point (with a smaller positive value). Thus, a saddle-center pair is generated at a definite value of a. The inner saddle gradually shifts closer to the event horizon, acquiring higher values of Ω^2, and finally one is left with a single saddle point through which physical monotransonic flow can occur. As in the case of polytropic flow, the value of parameter a at which the bifurcation occurs is different for different flow geometries, and that value is found to be minimum for disks in vertical hydrostatic equilibirum.

XV. SHOCK-INVARIANT QUANTITIES (S_h)

Applying the technique described in Sec. VI A, *shock-invariant quantities* (S_h) for all three isothermal flow geometries are obtained as follows.

A. Constant height flow

We have

$$S_h|^{iso}_{CH} = \left(\frac{u}{\sqrt{1-u^2}}\right)^{2c_s^2-1}(u^2\Delta + r^2c_s^2(1-u^2)). \quad (99)$$

B. Conical flow

We have

$$S_h|^{iso}_{CF} = \left(\frac{u}{\sqrt{1-u^2}}\right)^{2c_s^2-1}(u^2\Delta + r^2c_s^2(1-u^2)). \quad (100)$$

C. Flow in hydrostatic equilibrium in the vertical direction

We have

$$S_h|^{iso}_{VE} = u^{2c_s^2-1}(u^2\Delta + r^2c_s^2(1-u^2)). \quad (101)$$

XVI. SHOCK PARAMETER SPACE FOR ISOTHERMAL ACCRETION

We now intend to see which region of the $T-\lambda$ parameter space allows shock formation. For a fixed value of $a = 0.1$, we check the validity of the Rankine-Hugoniot condition for every value of $[T, \lambda]$ for which the accretion flow possesses three critical points. This means that the shock-invariant quantity is calculated for every $[T, \lambda]$ for which the multitransonic accretion is possible, and it is observed that only for some subset of such $[T, \lambda]$ do the shock-invariant quantities calculated along the solution passing through the outer and the inner sonic points become equal at a particular radial distance, i.e., at the shock location. We then plot the corresponding $[T, \lambda]_{shock}$ for various geometric configurations of matter.

In Fig. 18, we plot the subsets of the $T-\lambda$ spaces for three different flow geometries at a fixed a ($= 0.1$), for which the values of the shock-invariant quantities S_h, when evaluated along the flow branches through inner and outer critical points, become equal at particular values of r. This value of radial distance r_{sh} is the location of shock. The shaded region depicts the overlap of the shock-forming $[T, \lambda]$ parameter set of the three disk configurations for a given a.

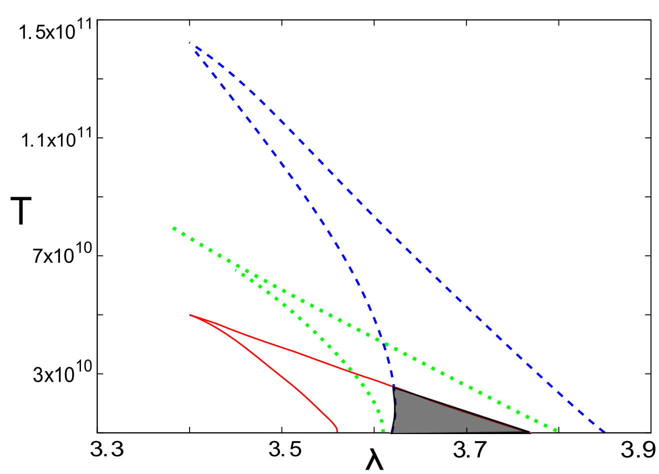

FIG. 18. Comparison of T-λ plots of allowed shocked multitransonic accretion solutions for three different flow geometries ($a = 0.1$, T in kelvins). Constant height disk, quasispherical flow, and flow in vertical hydrostatic equilibrium represented by blue dashed lines, green dotted lines, and red solid lines, respectively. Shaded region depicts the overlapping domain of shock formation in all three geometries.

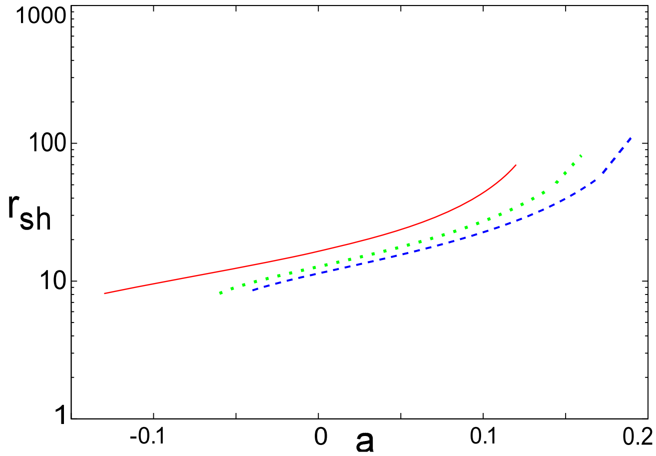

FIG. 19. Shock location (r_{sh}) vs a plot ($T = 10^{10}$ K, $\lambda = 3.75$) for a constant height disk (dashed blue line), quasispherical disk (dotted green line), and flow in hydrostatic equilibrium (solid red line).

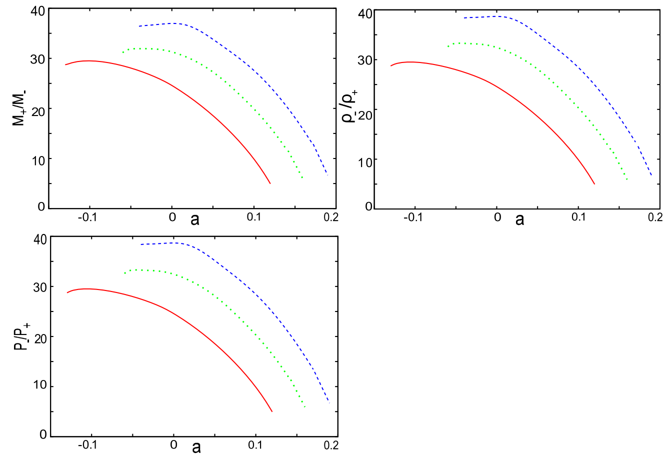

FIG. 20. Variation of shock strength (M_+/M_-), compression ratio (ρ_-/ρ_+), and pressure ratio (P_-/P_+) with black hole spin parameter a ($E = 10^{10}$ K, $\lambda = 3.75$) for a constant height flow (dashed blue lines), quasispherical flow (dotted green lines), and flow in hydrostatic equilibrium (solid red lines). The subscripts "+" and "−" represent pre- and postshock quantities, respectively.

Once the common region for shock formation is obtained, we investigate the variation of shock location (r_{sh}), shock strength (M_+/M_-), compression ratio (ρ_-/ρ_+), pressure ratio (P_-/P_+), and quasispecific energy dissipation ratio (ξ_+/ξ_-) (+ and − have the same meanings as defined for polytropic accretion) on the black hole spin parameter a, also comparing the trends of variation for various disk geometries.

Figure 19 shows how the shock location (r_{sh}) varies with the spin parameter a. The bulk ion temperature has been fixed at 10^{10} K, and the value of λ has been selected accordingly (3.75) from the region of shock overlap observed in Fig. 18 so that the available range of a is maximum. The same set of $[T, \lambda]$ has been used in all subsequent shock-related plots. As was already argued in the corresponding section for polytropic flow, the growth in strength of the effective centrifugal barrier due to the increase in the difference between λ and a explains the formation of shock farther away from the gravitating source as the value of black hole spin is increased while keeping the value of specific angular momentum fixed. Again, for a particular value of a, it is observed that $r_{sh}(VE) > r_{sh}(CF) > r_{sh}(CH)$, which indicates that even in the case of isothermal flow, an accretion disk in vertical hydrostatic equilibrium is exposed to maximum resistance for a given centrifugal barrier.

Figure 20, upon comparison with Fig. 11, establishes the fact that, irrespective of whether the flow is polytropic or isothermal, a gradual increase in black hole spin for a specific flow angular momentum shifts the shock location outward by boosting the effective centrifugal barrier. A shock formed far from the event horizon is weaker in strength owing to the eventual flattening of space-time. Moreover, in both polytropic and isothermal cases, for a given $[a, \lambda]$, the strongest shocks are formed in constant height disks, whereas disks in hydrostatic vertical equilibrium exhibit the weakest shocks. The same trend is consistently observed for all of the relevant ratios across the discontinuity.

XVII. POWERING THE FLARES THROUGH THE ENERGY DISSIPATED AT THE SHOCK

For the isothermal accretion onto a rotating black hole considered in this work, we concentrate on dissipative shocks. Unlike the standing Rankine-Hugoniot-type energy-preserving shocks studied for the polytropic flow, a substantial amount of energy is dissipated at the shock location to maintain the temperature invariance of the isothermal flow. As a consequence, the flow thickness does not change abruptly at the shock location, and handling the pressure balance equation across the shock becomes more convenient than that for the polytropic accretion. The amount of energy dissipated at the shock might make an isothermal shock appear "bright" since for the inviscid, dissipationless flow considered in our work, accretion remains grossly radiatively inefficient throughout.

The type of low angular momentum inviscid flow we consider in this work is believed to be ideal for mimicking the accretion environment of our Galactic Center black hole [34]. Sudden substantial energy dissipation from the shock surface may thus be conjectured to feed the x-ray and IR flares emanating from our Galactic Center black hole [103–111].

In our formalism, the ratios of the quasispecific energies corresponding to the preshock and postshock flows is assumed to be a measure of the amount of the dissipated energy at the shock surface. In Fig. 21, we plot such ratios

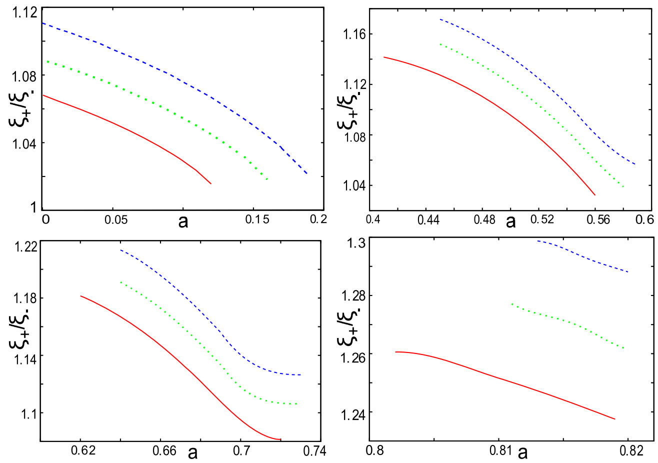

FIG. 21. Variation of quasispecific energy ratio (ξ_+/ξ_-) with black hole spin parameter a ($T = 10^{10}$ K). In order to obtain multicritical domains with shock over four different ranges of a, four different values of λ have been set at the given T, i.e., $\lambda = 3.75$ (upper left panel), $\lambda = 3.25$ (upper right panel), $\lambda = 3.0$ (lower left panel), $\lambda = 2.7$ (lower right panel). Constant height flow, quasispherical flow, and flow in hydrostatic equilibrium are represented by dashed blue lines, dotted green lines, and solid red lines. The subscripts "+" and "−" represent pre- and postshock quantities, respectively.

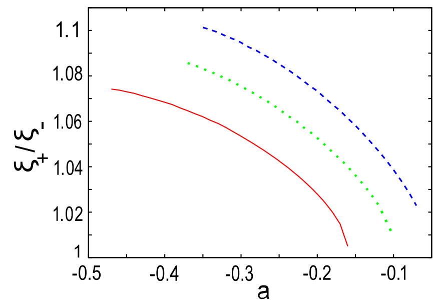

FIG. 22. Variation of quasispecific energy ratio (ξ_+/ξ_-) with black hole spin parameter a ($T = 10^{10}$ K, $\lambda = 4.0$) for retrograde flow. Constant height flow, quasispherical flow, and flow in hydrostatic equilibrium are represented by dashed blue lines, dotted green lines, and solid red lines. The subscripts "+" and "−" represent pre- and postshock quantities, respectively.

for various ranges of the black hole spins (the Kerr parameter a) for three different types of geometrical thickness of the flow considered in our work. There are four panels in the figure, with each plane corresponding to a certain range of values of the black hole spin angular momentum. As already discussed, for a fixed value of $[\mathcal{E}, \lambda, \gamma]$ or $[T, \lambda]$, shock formation over a continuous range of a spanning the entire domain of the Kerr parameter, $-1 > a > 1$, is allowed neither for polytropic nor for isothermal accretion. The four different panels in the figure are thus characterized by four different sets of $[T, \lambda]$, as mentioned in the figure caption. The following interesting features are observed.

Depending on the initial conditions, a substantial amount of energy gets liberated from the shock surface. Sometimes even as much as 30% of the rest mass may be converted into radiated energy, which is a huge amount. Hence, the shock-generated dissipated energy can, in principle, be considered a good candidate to explain the source of energy dumped into the flare.

The length scale on the disk from which the flare may be generated actually matches the shock location. Such "flare generating" length scales obtained in our theoretical calculations are thus in good agreement with observational works [109].

What we actually observe is that the amount of dissipated energy anticorrelates with the shock location, which is perhaps intuitively obvious because the closer the shock forms to the horizon, the greater is the available gravitational energy to be converted into dissipated radiation.

Following the same line of argument, the amount of dissipated energy anticorrelates with the flow angular momentum. The lower the angular momentum of the flow is, the closer to the boundary the centrifugal pressure supported region forms. Such regions slow down the flow and break the flow behind it, and hence the shock forms. The locations of such a region are thus markers anticipating from which region of the disk the flare may be generated.

It is imperative to study the influence of the black hole spin in determining the amount of energy liberated at the shock. What we find here is that, for the prograde flow, such an amount anticorrelates with the black hole spin. Thus, for a given flow angular momentum, slowly rotating black holes produce the strongest flares. Hence, for a given value of $[T, \lambda]$, if shocked multitransonic accretion solutions exist over a positive span of a including $a = 0$, then flares originating from the vicinity of the Schwarzschild hole would consequently contain the maximum amount of energy. Hence, unlike the Blandford-Znajek mechanism [38,112–115], the amount of energy transferred to a flare is not extracted at the expense of black hole spin.

Certain works based on the observational results argue that there is no obvious correlation between the black hole spin and the jet power (see Refs. [116,117] and the references therein). Our present finding is in accordance with such arguments.

In this connection, however, it is to be noted that the Blandford-Znajek mechanism is usually associated with the electromagnetic energy extractions, whereas energy liberation at the shock is associated with the hydrodynamic flow. Hence, no direct comparison can perhaps be made between the Blandford-Znajek process and the process considered in our work.

In recent years, the study of retrograde flow close to the Kerr holes has also been of profound interest (see Refs. [118,119] and the references therein). We thus study the spin dependence of the amount of energy dissipation at the shock. The result is shown in Fig. 22. Here we observe that the amount of dissipated energy is greater for faster *counterrotating* holes. For retrograde flow, the negative Kerr parameter essentially reduces the overall measure of the angular momentum of the flow and the effective angular momentum may probably be thought of as $\lambda_{eff} = \lambda - a$, which explains such a finding.

It is also observed that the amount of shock dissipated energy is also influenced by the geometric configuration of the flow. We find that axially symmetric flow with constant thickness produces the largest amount of liberated energy at the shock, whereas the flow in hydrostatic equilibrium along the vertical direction produces the smallest amount. The conical wedge-shaped flow contributes at a rate which is intermediate to the rates for the constant height disk and the disk in vertical equilibrium. This feature remains unaltered for the prograde as well as the retrograde flow.

XVIII. QUASITERMINAL VALUES

A. Dependence of $[M,\rho,P]_{r_\delta}$ on a for shocked isothermal accretion

Variation of the quasiterminal values of Mach number (M_δ), density (ρ_δ), and pressure (P_δ) with spin parameter a is shown in Fig. 23 for a given T ($= 10^{10}$ K) and λ ($= 3.75$). It is observed that the variations are similar in nature to those for polytropic flow, but even in this case, limitations in the availability and overlap of a broad range of spin for shocked multitransonic accretion for all geometric models make it impossible to comment on the global trend with which such quantities vary in accordance to black hole spin or the disk configuration. Hence, we try to resolve this issue in the next subsection by looking at the case of monotransonic isothermal accretion.

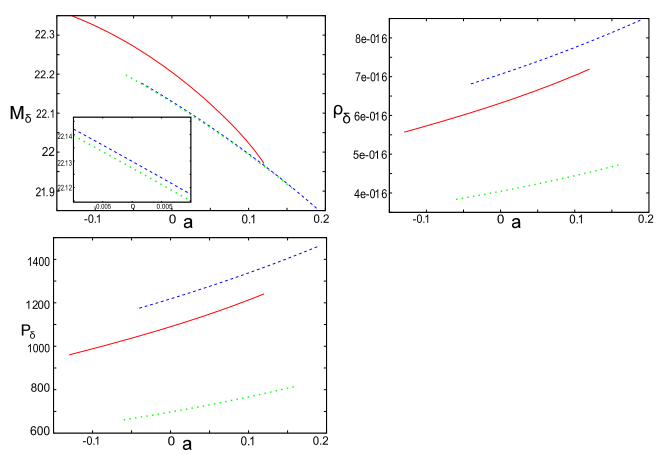

FIG. 23. Variation of quasiterminal values of Mach number (M_δ), density (ρ_δ), and pressure (P_δ) with a ($T = 10^{10}$ K, $\lambda = 3.75$) for constant height flow (dashed blue lines), quasi-spherical flow (dotted green lines), and flow in hydrostatic equilibrium (solid red lines). Density and pressure are in cgs units of $\mathrm{g\,cm^{-3}}$ and $\mathrm{dyn\,cm^{-2}}$, respectively, and temperature is in absolute units of kelvin.

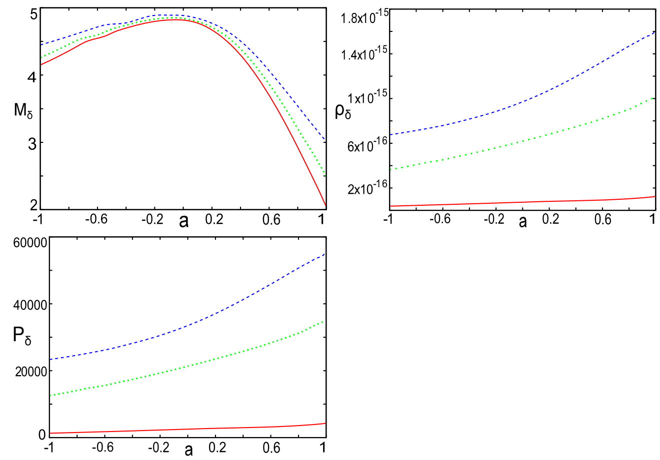

FIG. 24. Variation of quasiterminal values of Mach number (M_δ), density (ρ_δ), and pressure (P_δ) with a ($T = 2 \times 10^{11}$ K, $\lambda = 2.0$) for monotransonic accretion in constant height flow (dashed blue lines), quasispherical flow (dotted green lines), and flow in hydrostatic equilibrium (solid red lines). Density and pressure are in cgs units of $\mathrm{g\,cm^{-3}}$ and $\mathrm{dyn\,cm^{-2}}$, respectively, and temperature is in absolute units of kelvin.

B. Dependence of $[M,\rho,P]_{r_\delta}$ on a for monotransonic isothermal accretion

Figure 24 depicts how quasiterminal values of Mach number, density, and pressure of monotransonic isothermal flow depend on the Kerr parameter. Hot flows with low angular momentum exhibit stationary accretion solutions spanning the full domain of black hole spin. It is observed that the general spin-dependent behavior of the corresponding physical quantities for three different flow geometries is quite well behaved in the case of isothermal accretion, as opposed to the polytropic case. However, the previously stated intrinsic limitations in the possibility of observing variations over the complete range of spin still exist for multitransonic flows. It is clear from Fig. 24 that quasiterminal values possess common global trends of variation over a for all three geometric configurations. The important observation in this context is the existence of asymmetry in variation of the related quantities between prograde and retrograde spin of the black hole. As mentioned in the case of polytropic accretion, such asymmetry is an extremely significant finding for the observation of black hole spin-related effects.

XIX. CONCLUDING REMARKS

Computation of the quasiterminal values helps us to understand the nature of spectra for which photons have emanated from a close proximity of the horizon. Hence, variation of the quasiterminal values may be useful to understand how the black hole spin influences the configuration of the image of the black hole shadow. This work has put forth two important findings which are worth mentioning in this context. Firstly, the spin dependence of quasiterminal values has been studied for different geometrical configurations of matter. Secondly, we have found that (see, e.g., Figs. 13 and 24) the prograde and the retrograde flows are distinctly marked by asymmetric distributions of relevant quasiterminal values over the entire theoretical range of the Kerr parameter. This indicates that the constructed image of shadow will be different for the co- and counterrotating flows. We have also observed that the physical quantities responsible for constructing the black hole spectra [velocity, density, pressure, temperature (for polytropic accretion), and quasispecific energy (for isothermal accretion) of the flow] change abruptly at the shock location. This indicates that the discontinuous changes in the physical quantities should be manifested as a break in the corresponding spectral index, and they will also show up during the procedure of black hole shadow imaging. Our work is thus expected to predict how the shape of the image of the shadow might be governed by the dynamical and thermodynamic properties of the accretion flow along with the spin of a black hole. Through the construction of such an image (a work in progress), not only shall we be able to provide a possible methodology (at least at a qualitative level) for the observational signature of the black hole spin, but such images will also possibly shed light on the difference between the prograde and retrograde flows from an observational point of view. We have analyzed general relativistic accretion of both polytropic and isothermal fluids in the Kerr metric to study the effects of matter geometry and black hole spin parameter on multitransonic shocked accretion flow.

ACKNOWLEDGMENTS

P. T. would like to acknowledge the financial and infrastructural support provided by S. N. Bose National Centre for Basic Sciences, Department of Science and Technology, Government of India, for this work. P. T. and S. N. would like to acknowledge the kind hospitality provided by Harish-Chandra Research Institute (HRI), HBNI, Department of Atomic Energy, Government of India, for several visits through the XIIth plan budget of Cosmology and High Energy Astrophysics grant. The long-term visiting student position of D. A. B. at HRI was supported by the aforementioned grant as well. The authors would like to thank Sonali Saha Nag for her kind help in formulating an initial version of the numerical code that has been partially used in this work. T. K. D. acknowledges the support provided by Physics and Applied Mathematics Unit, Indian Statistical Institute, Government of India (in the form of a long-term visiting scientist position), where parts of this work were carried out. P. T. feels happy to acknowledge the insightful discussions with Prof. Amitabha Lahiri. The authors thank the anonymous referees for the thoughtful comments and useful suggestions which helped to improve the manuscript.

[1] J. Frank, A. King, and D. Raine, *Accretion Power in Astrophysics*, Vol. 21 (Cambridge University Press, Cambridge, England, 1992).
[2] I. Novikov and K. S. Thorne, in *Black Holes*, edited by C. De Witt and B. De Witt (Gordon and Breach, New York, 1973).
[3] E. P. T. Liang and K. A. Thomson, Astrophys. J. **240**, 271 (1980).
[4] M. A. Abramowicz and W. H. Zurek, Astrophys. J. **246**, 314 (1981).
[5] B. Muchotrzeb and B. Paczynski, Acta Astron. **32**, 1 (1982).
[6] J. Fukue, Publ. Astron. Soc. Jpn. **35**, 355 (1983).
[7] J. F. Lu, Astron. Astrophys. **148**, 176 (1985).
[8] J. F. Lu, Gen. Relativ. Gravit. **18**, 45L (1986).
[9] B. Muchotrzeb-Czerny, Acta Astron. **36**, 1 (1986).
[10] O. Blaes, Mon. Not. R. Astron. Soc. **227**, 975 (1987).
[11] S. K. Chakrabarti, Astrophys. J. **347**, 365 (1989).
[12] K. Nakayama and J. Fukue, Publ. Astron. Soc. Jpn. **41**, 271 (1989).
[13] M. A. Abramowicz and S. Kato, Astrophys. J. **336**, 304 (1989).
[14] M. A. Abramowicz and S. K. Chakrabarti, Astrophys. J. **350**, 281 (1990).
[15] M. Takahashi, D. Rilett, K. Fukumura, and S. Tsuruta, Astrophys. J. **572**, 950 (2002).
[16] M. Kafatos and R. X. Yang, Mon. Not. R. Astron. Soc. **268**, 925 (1994).
[17] H. Sponholz and D. Molteni, Mon. Not. R. Astron. Soc. **271**, 233 (1994).
[18] R. Yang and M. Kafatos, Astron. Astrophys. **295**, 238 (1995).
[19] V. I. Pariev, Mon. Not. R. Astron. Soc. **283**, 1264 (1996).
[20] K. Nakayama, Mon. Not. R. Astron. Soc. **281**, 226 (1996).
[21] S. K. Chakrabarti, Astrophys. J. **471**, 237 (1996).
[22] S. K. Chakrabarti, Mon. Not. R. Astron. Soc. **283**, 325 (1996).
[23] J. Peitz and S. Appl, Mon. Not. R. Astron. Soc. **286**, 681 (1997).
[24] H. J. Bussemaker, D. Thirumalai, and J. K. Bhattacharjee, Phys. Rev. Lett. **79**, 3530 (1997).
[25] G. Tóth, R. Keppens, and M. A. Botchev, Astron. Astrophys. **332**, 1159 (1998).
[26] S. K. Chakrabarti and S. Das, Mon. Not. R. Astron. Soc. **327**, 808 (2001).
[27] T. K. Das, Astrophys. J. **577**, 880 (2002).

[28] T. K. Das, J. K. Pendharkar, and S. Mitra, Astrophys. J. **592**, 1078 (2003).
[29] K. Fukumara and S. Tsuruta, Astrophys. J. **611**, 964 (2004).
[30] T. Okuda, V. Teresi, E. Toscano, and D. Molteni, Publ. Astron. Soc. Jpn. **56**, 547 (2004).
[31] P. Barai, T. K. Das, and P. J. Wiita, Astrophys. J. Lett. **613**, L49 (2004).
[32] J. Fukue, Publ. Astron. Soc. Jpn. **56**, 959 (2004).
[33] J. Fukue, Publ. Astron. Soc. Jpn. **56**, 681 (2004).
[34] M. Moscibrodzka, T. K. Das, and B. Czerny, Mon. Not. R. Astron. Soc. **370**, 219 (2006).
[35] M. Takahashi, J. Goto, K. Fukumura, D. Rilett, and S. Tsuruta, Astrophys. J. **645**, 1408 (2006).
[36] H. Nagakura and S. Yamada, Astrophys. J. **689**, 391 (2008).
[37] H. Nagakura and S. Yamada, Astrophys. J. **696**, 2026 (2009).
[38] T. K. Das and B. Czerny, Mon. Not. R. Astron. Soc. **421**, L24 (2012).
[39] T. K. Das, S. Nag, S. Hegde, S. Bhattacharya, I. Maity, B. Czerny, P. Barai, P. J. Wiita, V. Karas, and T. Naskar, New Astron. **37**, 81 (2015).
[40] K. Akiyama, A. Alberdi, W. Alef, K. Asada, R. Azulay, A.-K. Baczko, D. Ball, M. Baloković, J. Barrett *et al.* (Event Horizon Telescope Collaboration), Astrophys. J. Lett. **875**, L1 (2019).
[41] K. Akiyama, A. Alberdi, W. Alef, K. Asada, R. Azulay, A.-K. Baczko, D. Ball, M. Baloković, J. Barrett *et al.* (Event Horizon Telescope Collaboration), Astrophys. J. Lett. **875**, L2 (2019).
[42] K. Akiyama, A. Alberdi, W. Alef, K. Asada, R. Azulay, A.-K. Baczko, D. Ball, M. Baloković, J. Barrett *et al.* (Event Horizon Telescope Collaboration), Astrophys. J. Lett. **875**, L3 (2019).
[43] K. Akiyama, A. Alberdi, W. Alef, K. Asada, R. Azulay, A.-K. Baczko, D. Ball, M. Baloković, J. Barrett *et al.* (Event Horizon Telescope Collaboration), Astrophys. J. Lett. **875**, L4 (2019).
[44] K. Akiyama, A. Alberdi, W. Alef, K. Asada, R. Azulay, A.-K. Baczko, D. Ball, M. Baloković, J. Barrett *et al.* (Event Horizon Telescope Collaboration), Astrophys. J. Lett. **875**, L5 (2019).
[45] K. Akiyama, A. Alberdi, W. Alef, K. Asada, R. Azulay, A.-K. Baczko, D. Ball, M. Baloković, J. Barrett *et al.* (Event Horizon Telescope Collaboration), Astrophys. J. Lett. **875**, L6 (2019).
[46] F. Melia, Astrophys. J. **387**, L25 (1992).
[47] F. Melia, S. Liu, and R. Coker, Astrophys. J. **553**, 146 (2001).
[48] M. Moscibrodzka, Astron. Astrophys. **450**, 93 (2006).
[49] B. Czerny, M. Mościbrodzka, D. Proga, T. K. Das, and A. Siemiginowska, in *Proceedings of RAGtime 8/9: Workshops on Black Holes and Neutron Stars, Opava, Czech Republic, 2007*, edited by S. Hledík and Z. Stuchlík (Silesian University in Opava, Opava, Czech Republic, 2007), pp. 35–44.
[50] D. P. Marrone, J. M. Moran, J.-H. Zhao, and R. Rao, Astrophys. J. **654**, L57 (2007).
[51] A. M. Ghez, S. Salim, N. N. Weinberg, J. R. Lu, T. Do, J. K. Dunn, K. Matthews, M. R. Morris, S. Yelda, E. E. Becklin, T. Kremenek, M. Milosavljevic, and J. Naiman, Astrophys. J. **689**, 1044 (2008).
[52] S. Gillessen, F. Eisenhauer, T. K. Fritz, H. Bartko, K. Dodds-Eden, O. Pfuhl, T. Ott, and R. Genzel, Astrophys. J. **707**, L114 (2009).
[53] K. Ferrière, Astron. Astrophys. **505**, 1183 (2009).
[54] R. Genzel, F. Eisenhauer, and S. Gillessen, Rev. Mod. Phys. **82**, 3121 (2010).
[55] T. Okuda and D. Molteni, Mon. Not. R. Astron. Soc. **425**, 2413 (2012).
[56] A. K. Ray and J. K. Bhattacharjee, Phys. Rev. E **66**, 066303 (2002).
[57] N. Afshordi and B. Paczyński, Astrophys. J. **592**, 354 (2003).
[58] S. Chaudhury, A. K. Ray, and T. K. Das, Mon. Not. R. Astron. Soc. **373**, 146 (2006).
[59] I. Mandal, A. K. Ray, and T. K. Das, Mon. Not. R. Astron. Soc. **378**, 1400 (2007).
[60] R. Matsumoto, S. Kato, J. Fukue, and A. T. Okazaki, Publ. Astron. Soc. Jpn. **36**, 71 (1984).
[61] T. Bohr, P. Dimon, and V. Putkaradze, J. Fluid Mech. **254**, 635 (1993).
[62] J. M. Miller, C. S. Reynolds, A. C. Fabian, G. Miniutti, and L. C. Gallo, Astrophys. J. **697**, 900 (2009).
[63] T. Dauser, J. Wilms, C. S. Reynolds, and L. W. Brenneman, Mon. Not. R. Astron. Soc. **409**, 1534 (2010).
[64] Y. Kato, M. Miyoshi, R. Takahashi, H. Negoro, and R. Matsumoto, Mon. Not. R. Astron. Soc. **403**, L74 (2010).
[65] A. Tchekhovskoy, R. Narayan, and J. C. McKinney, Astrophys. J. **711**, 50 (2010).
[66] J. Ziolkowski, Mem. Soc. Astron. Ital. **81**, 294 (2010).
[67] S. D. Buliga, V. I. Globina, Y. N. Gnedin, T. M. Natsvlishvili, M. Y. Pitrovich, and N. A. Shakht, Astrophysics **54**, 548 (2011).
[68] R. A. Daly, Mon. Not. R. Astron. Soc. **414**, 1253 (2011).
[69] A. Martínez-Sansigre and S. Rawlings, Mon. Not. R. Astron. Soc. **414**, 1937 (2011).
[70] J. E. McClintock, R. Narayan, S. W. Davis, L. Gou, A. Kulkarni, J. A. Orosz, R. F. Penna, R. A. Remillard, and J. F. Steiner, Classical Quantum Gravity **28**, 114009 (2011).
[71] C. J. Nixon, P. J. Cossins, A. R. King, and J. E. Pringle, Mon. Not. R. Astron. Soc. **412**, 1591 (2011).
[72] C. S. Reynolds, L. W. Brenneman, A. M. Lohfink, M. L. Trippe, J. M. Miller, R. C. Reis, M. A. Nowak, and A. C. Fabian, AIP Conf. Proc. **1427**, 157 (2012).
[73] A. Tchekhovskoy and J. C. McKinney, Mon. Not. R. Astron. Soc. **423**, L55 (2012).
[74] L. Brenneman, *Measuring the Angular Momentum of Supermassive Black Holes*, Springer Briefs in Astronomy (Springer, New York, 2013), p. 978.
[75] M. Dotti, M. Colpi, S. Pallini, A. Perego, and M. Volonteri, Astrophys. J. **762**, 68 (2013).
[76] J. C. McKinney, A. Tchekhovskoy, and R. D. Blandford, Science **339**, 49 (2013).
[77] A. C. Fabian, M. L. Parker, D. R. Wilkins, J. M. Miller, E. Kara, C. S. Reynolds, and T. Dauser, Mon. Not. R. Astron. Soc. **439**, 2307 (2014).

[78] J. Healy, C. O. Lousto, and Y. Zlochower, Phys. Rev. D **90**, 104004 (2014).
[79] J. Jiang, C. Bambi, and J. F. Steiner, J. Cosmol. Astropart. Phys. 05 (2015) 025.
[80] R. S. Nemmen and A. Tchekhovskoy, Mon. Not. R. Astron. Soc. **449**, 316 (2015).
[81] A. Sesana, E. Barausse, M. Dotti, and E. M. Rossi, Astrophys. J. **794**, 104 (2014).
[82] P. Mach, M. Piróg, and J. A. Font, Classical Quantum Gravity **35**, 095005 (2018).
[83] F. D. Lora-Clavijo, A. Cruz-Osorio, and E. M. Méndez, Astrophys. J. Suppl. Ser. **219**, 30 (2015).
[84] A. Cruz-Osorio and F. D. Lora-Clavijo, Mon. Not. R. Astron. Soc. **460**, 3193 (2016).
[85] A. Cruz-Osorio, F. J. Sánchez-Salcedo, and F. D. Lora-Clavijo, Mon. Not. R. Astron. Soc. **471**, 3127 (2017).
[86] H. Riffert and H. Herold, Astrophys. J. **450**, 508 (1995).
[87] M. A. Abramowicz, X. M. Chen, M. Granath, and J. P. Lasota, Astrophys. J. **471**, 762 (1996).
[88] M. A. Abramowicz, A. Lanza, and M. J. Percival, Astrophys. J. **479**, 179 (1997).
[89] N. Bilić, A. Choudhary, T. K. Das, and S. Nag, Classical Quantum Gravity **31**, 035002 (2014).
[90] S. Goswami, S. N. Khan, A. K. Ray, and T. K. Das, Mon. Not. R. Astron. Soc. **378**, 1407 (2007).
[91] D. W. Jordan and P. Smith, *Nonlinear Ordinary Differential Equations* (Oxford University Press, Oxford, 1999).
[92] P. Tarafdar and T. K. Das, New Astron. **62**, 1 (2018).
[93] B. Paczyński and P. J. Wiita, Astron. Astrophys. **88**, 23 (1980).
[94] D. A. Bollimpalli, S. Bhattacharya, and T. K. Das, New Astron. **51**, 153 (2017).
[95] Heteroclinic orbits are the trajectories defined on a phase portrait which connects two different saddle-type critical points. Integral solution configurations on a phase portrait characterized by heteroclinic orbits are topologically unstable [see Ref. [91] and S. H. Strogatz, *Nonlinear Dynamics and Chaos: With Applications to Physics, Biology, Chemistry, and Engineering* (Westview Press, Boulder, CO, 2001)].
[96] H. Falcke, F. Melia, and E. Agol, AIP Conf. Proc. **522**, 317 (2000).
[97] R. Takahashi, in *Proceedings of International Astronomical Union Symposium 222: The Interplay among Black Holes, Stars and ISM in Galactic Nuclei*, edited by T. S. Bergmann, L. C. Ho, and H. R. Schmitt (Cambridge University Press, Cambridge, England, 2004), p. 115.
[98] L. Huang, M. Cai, Z. Q. Shen, and F. Yuan, Mon. Not. R. Astron. Soc. **379**, 833 (2007).
[99] K. Hioki and K.-I. Maeda, Phys. Rev. D **80**, 024042 (2009).
[100] A. F. Zakharov, F. D. Paolis, G. Ingrosso, and A. A. Nucita, New Astron. Rev. **56**, 64 (2012).
[101] O. Straub, F. H. Vincent, M. A. Abramowicz, E. Gourgoulhon, and T. Paumard, Astron. Astrophys. **543**, A83 (2012).
[102] A. A. Esin, J. E. McClintock, and R. Narayan, Astrophys. J. **489**, 865 (1997).
[103] F. K. Baganoff, M. W. Bautz, W. N. Brandt, G. Chartas, E. D. Feigelson, G. P. Garmire, Y. Maeda, M. Morris, G. R. Ricker, L. K. Townsley, and F. Walter, Nature (London) **413**, 45 (2001).
[104] R. Genzel, R. Schödel, T. Ott, A. Eckart, T. Alexander, F. Lacombe, D. Rouan, and B. Aschenbach, Nature (London) **425**, 934 (2003).
[105] D. P. Marrone, F. K. Baganoff, M. R. Morris, J. M. Moran, A. M. Ghez, S. D. Hornstein, C. D. Dowell, D. J. Muñoz, M. W. Bautz, G. R. Ricker, W. N. Brandt, G. P. Garmire, J. R. Lu, K. Matthews, J. H. Zhao, R. Rao, and G. C. Bower, Astrophys. J. **682**, 373 (2008).
[106] B. Czerny, P. Lachowicz, M. Dovčiak, V. Karas, T. Pecháček, and T. K. Das, Astron. Astrophys. **524**, A26 (2010).
[107] Q. D. Wang, M. A. Nowak, S. B. Markoff, F. K. Baganoff, S. Nayakshin, F. Yuan, J. Cuadra, J. Davis, J. Dexter, A. C. Fabian, N. Grosso, D. Haggard, J. Houck, L. Ji, Z. Li, J. Neilsen, D. Porquet, F. Ripple, and R. V. Shcherbakov, Science **341**, 981 (2013).
[108] G. Ponti, B. De Marco, M. R. Morris, A. Merloni, T. Muñoz-Darias, M. Clavel, D. Haggard, S. Zhang, K. Nandra, S. Gillessen, K. Mori, J. Neilsen, N. Rea, N. Degenaar, R. Terrier, and A. Goldwurm, Mon. Not. R. Astron. Soc. **454**, 1525 (2015).
[109] G. D. Karssen, M. Bursa, A. Eckart, M. Valencia-S, M. Dovčiak, V. Karas, and J. Horák, Mon. Not. R. Astron. Soc. **472**, 4422 (2017).
[110] E. Mossoux and N. Grosso, Astron. Astrophys. **604**, A85 (2017).
[111] Q. Yuan, Q. D. Wang, S. Liu, and K. Wu, Mon. Not. R. Astron. Soc. **473**, 306 (2018).
[112] R. D. Blandford and R. L. Znajek, Mon. Not. R. Astron. Soc. **179**, 433 (1977).
[113] M. O'Riordan, A. Pe'er, and J. C. McKinney, Astrophys. J. **831**, 62 (2016).
[114] B. Czerny and B. You, Astron. Nachr. **337**, 73 (2016).
[115] C. Bambi, Rev. Mod. Phys. **89**, 025001 (2017).
[116] R. P. Fender, E. Gallo, and D. Russell, Mon. Not. R. Astron. Soc. **406**, 1425 (2010).
[117] J. W. Broderick and R. P. Fender, Mon. Not. R. Astron. Soc. **417**, 184 (2011).
[118] D. Garofalo, Adv. Astron. **2013**, 213105 (2013).
[119] A. G. Mikhailov, M. Y. Piotrovich, Y. N. Gnedin, T. M. Natsvlishvili, and S. D. Buliga, Mon. Not. R. Astron. Soc. **476**, 4872 (2018).